Optical Nanoantennas Integrated with 3D Microelectrode Arrays: Hybrid Photonic-Electronic Modalities for Nano-Bio Interfacing

Elieser A. Mejia

Thesis submitted to the faculty of the Virginia Polytechnic Institute and State University
in partial fulfillment of the requirements for the degree of

Master of Science
In
Electrical Engineering

Wei Zhou, Chair
Xiaoting Jia, Member
Guoqiang Yu, Member

November 8, 2024
Blacksburg, Virginia

Keywords: optoelectrode, plasmonics, biosensors, nanofabrication, bio-nano interface, multi-electrode arrays, nano-optics, bio-photonics, micropillars

Optical Nanoantennas Integrated with 3D Microelectrode Arrays: Hybrid Photonic-Electronic Modalities for Nano-Bio Interfacing

Elieser A. Mejia

ABSTRACT

The development of advanced devices and systems to quantify dynamic biological phenomena across molecular, cellular, and tissue scales is needed to understand complex interwoven biochemical and bioelectrical cellular dynamics. New technologies must enable precise measurement of biomolecular gradients, cellular properties, and tissue-level responses, supporting innovations in fields such as organ-on-chip systems, flow cytometry, wearable devices, and implantable sensors. Building towards such applications, we introduce fixed-size tapered nanolaminate nanoantennas (TNLNAs) as a novel nanophotonic platform leveraging a multiresonant plasmonic responses. These optical nanoantennas, engineered with tunable metal-to-insulator thickness ratios, achieve wide double-resonance spectral tunability, critical for achieving desired optical properties while maintained a fixed geometry for controlled cellular responses at the nano-bio interface. TNLNAs fabricated via a high-throughput nanofabrication method exhibit resonant wavelengths tunable between 730–1050 nm, offering up to 1000-fold near-field intensity enhancements through a bianisotropy-induced magnetoelectric responses. This tunability enables spatial overlap between electric and magnetic polarizabilities, evoking higher-order multipolar behaviors and broadening their application in nano-optic operations and cellular interfacing. Expanding on these capabilities, we demonstrate a hierarchical modular approach to fabricate two-tier protruding micro-/nano-optoelectrode arrays, consisting of 3D micropillar electrode arrays integrated with TNLNAs, providing electronic and photonic functionality designed for in situ spatiotemporal characterization of living multicellular systems. These multifunctional arrays combine plasmonic nanoantenna-based biophotonics for surface-enhanced Raman spectroscopy (SERS) and bioelectronic modalities for electrochemical impedance spectroscopy (EIS). By coupling biomimetic micro-/nano-pillar topographies with scalable nanocavity modes, the arrays achieve high SERS enhancement factors (~10^6) and reduced interfacial impedance, enabling correlated bioelectrical-biochemical measurements. This platform holds promise for applications in neuronal networks, cancer organoids, and microbial biofilms, offering transformative potential in biology and medicine.

Optical Nanoantennas Integrated with 3D Microelectrode Arrays: Hybrid Photonic-Electronic Modalities for Nano-Bio Interfacing

Elieser A. Mejia

GENERAL AUDIENCE ABSTRACT

The human body is dynamic and understanding such complexity for accurate diagnostics and therapies remains a challenge due to lack of minimally-invasive biotechnologies capable of long-term measurements of various biochemical and bioelectrical signals simultaneously from single cells to cell networks. Biocompatibility is a major challenge but recent advancements in micro- and nano-fabrication has shown that patterned protruding pillars from surfaces at the micro- and nano-scale can mimic intrinsic biological structural cues to trigger strong cell adhesion, engulfment, and growth, providing a means by which to engineer the biocompatibility for controlled cell-device bio-interfaces. Here, we sought to leverage the unique biocompatibility of engineered three-dimensional (3D) features with integrated biochemical and bioelectrical sensor arrays to create a multi-modal platform for complex systems biological research. For the biochemical sensor, we introduced a tunable optical nanoantenna that is driven wirelessly by incident laser light (photons) to create a highly localized electric field capable of enhancing the photon scattering rate of nearby chemical bonds, a unique signature that provides a means to fingerprint the local biomolecular ensembles depending on the color of detected scattered photons. By a novel scalable fabrication technique, we merged such nano-sensors with 3D micropillar electrode arrays to create a device with hybrid biophotonic and bioelectronic functionality. We revealed the unique optical properties by micro-reflectance measurements and numerical simulations and verified by spectroscopic measurements a million-fold enhancement to the scattered photon signature from a standard chemical monolayer. We showed favorable bioelectrical properties by electrochemical impedance spectroscopy and cyclic voltammetry, revealing a stable electrochemical interface and reduced resistance due to 3D geometry enabling improved transduction of electrical signals, useful for higher signal to noise ratios in bioelectrical measurements. Overall, we demonstrated the scalable fabrication and unique optical and electrical properties suitable for next generation multi-modal bio-interfacing platforms.

Dedication

This is dedicated to all the teachers and professors who recognized and helped me realize my potential. In particular this is dedicated to my high school chemistry teacher, Jodie Molchany and my high school engineering teacher John Ensor. I faced many challenges growing up, and was indifferent to schooling, but Ms. Molchany and Mr. Ensor were incredibly patient with me and helped me realize my true potential.

Acknowledgements

This work and EM was supported by the Center for Nanoscale Science and Technology (CNST) at the National Institute of Standards and Technology (NIST) as part of a summer undergraduate research fellowship in 2019. Device fabrication, dark-field scattering, micro-reflectance, and micro-transmissions measurements were completed at NIST by EM, under training and supervision of Amit Agrawal, Jared Strait, Wenqi Zhu, Junyeob Song, and the CNST staff. Devices were further characterized at VT via SERS, electrochemical impedance spectroscopy, and cyclic voltammetry by EM, under training and supervision of Chaun Xiao, Meitong Nie, and Wei Zhou.

Table of Contents

List of Figures

Chapter 1. Introduction

An enhanced understanding and further advancements in medicine and personalized point-of-healthcare in the 21^{st} are currently hindered by the inherent challenges of deciphering complex interwoven biological processes spanning various subsystems across wide spatial and temporal scales. Monitoring in real time the constituents of such subsystems, either ex vivo, in vivo, or in vitro, in response to certain perturbations possess technical challenges due to the lack of devices capable of extracting biophysical-chemical-electrical information with adequate spatiotemporal resolutions while preserving the native state of the biological (sub) system. Addressing such challenges first necessitates avoiding the triggering of biological defense mechanisms involving foreign body detection as part of the immune system. Such biological response mechanisms can be evaded by mimicking the intrinsic structural and chemical characteristic features of soft matter and biological physics. One method to evade detection is by incorporating micro- and nano-scale surface features, biological surface chemistry, flexible/soft polymers, and corrosion-resistant materials that avoid long-term degradation. The next challenges centers on creating miniaturized devices that can transduce local cellular activity, specifically bio-molecular and bio-electrical, to a detectable external signal. Gold nanostructures pose as a suitable device as gold is highly non-reactive and the size and geometrical features of nanostructures leads to novel light-mater interactions that can be leveraged for a variety of transduction pathways useful for bio-interface control and monitoring. The surface-confinement of optical fields in nanoscale geometries enhances multiple interfacial light scattering processes of molecules and atoms, providing a detectable signal source for continuous monitoring. Another important bio-signal of interest is the electrical impulses of electrogenic cells which is routinely and reliably monitored by metal “electrodes”. Such conventional electrode technology has matured but the integration of micro- and nano-electrodes with optically resonant nanostructures remains unaddressed despite serving as a promising avenue for advanced multi-modal bio-interface technology. Therefore, merging three-dimensional micro-electrodes and gold nanostructures can potentially provide a viable pathway for co-localized monitoring of bio-molecular and bio-electrical information to study a diverse set of biological subsystems in an minimally invasive manner over long periods of time. This thesis explores the device physics and integration of a certain class of composite nanostructures and their favorable optical properties suitable for aforementioned bio-applications and their integration with biomimetic electrode surfaces, setting the foundation for the next generation of advanced bio-interfacing devices.

Chapter 2. Spectral Tuning of Double Resonant Nanolaminate Plasmonic Nanoantennas with a Fixed Size

(This chapter has been published in Applied Physics Letters.[1] This paper is published by American Institute of Physics)

2.1 Abstract

Multiresonant plasmonic nanoantennas can enhance nanolocalized multiphoton processes or enable wavelength-multiplexed nano-optic operations by supporting multiple spatially overlapped plasmonic modes at various wavelength bands. Nevertheless, current multiresonant plasmonic nanoantenna designs do not consider engineering multiresonant spectral responses with strict size and footprint constraints. Developing a strategy to engineer fixed-size nanoantennas with tunable multiresonant responses is highly desirable for maintaining controlled cellular responses at the bio-nano interface and achieving seamless integration with other nanodevices with predefined footprints. Here, we report that fixed-size tapered nanolaminate nanoantennas (TNLNAs) can achieve a wide double-resonance spectral tunability by only changing the metal-to-insulator thickness ratio (t/h). Three separate TNLNAs samples (8nm/38nm, 20nm/20nm, 28nm/8nm) with a nominal total height of ~100nm are created from a high-throughput nanofabrication technique. Specifically, we fabricated TNLNAs samples by exploiting a nanohole array membrane from soft interference lithography as a deposition mask for electron-beam evaporation of alternating Au and SiO_2 layers. Transmission and dark field scattering measurements show that TNLNAs support two distinct resonant features with t/h-dependent tunable resonant wavelengths in the range of 730-850 nm and 840-1050 nm, respectively. Numerical simulations reveal that (i) bianisotropy-induced magnetoelectric response in top and bottom nanogaps due to the asymmetric tapered shape can enhance light trapping and achieve optical near-field intensity enhancements up to 1000-fold; (ii) while TNLNAs consisting of thin Au nanodisks at low t/h primarily support spatial overlap between modes with enhanced electric polarizability, TNLNAs consisting of thick Au nanodisks at high t/h primarily support spatial overlap between modes with enhanced magnetic polarizability to show higher-order multipolar behaviors.

2.2 Introduction

Plasmonic nanoantennas (PNAs) can support localized surface plasmon (LSP) modes to concentrate and transduce optical energy at deep subwavelength scales.[2-7] PNAs with optimized single-resonant near-field characteristics are sufficient for applications based on single-photon excitation/emission processes', such as photothermal conversion, hot carrier generation, elastic/inelastic scattering, and photoluminescence.[8-10] However, for applications based on multiphoton processes or wavelength-multiplexed operations, it is highly desirable to engineer multiresonant PNAs to enhance nanolocalized optical processes in two or more wavelength bands.[11] Currently, there are several strategies to engineer the multiresonant response of PNAs. First, PNAs of high aspect ratios and large sizes can support multiple high-order modes from phase retardation effects.[12, 13] Second, planar composite PNAs consisting of optically coupled plasmonic nanoresonators can support multiple hybridized LSP modes,[14-17] Third, core-shell PNAs can support multiple hybridized LSP modes at multiple metal-dielectric interfaces.[18-21] Whether relying on near-field interactions or a collection of self-similar yet different sized plasmonic building blocks, engineering and structurally tuning the multiresonant response typically involves changing the physical size/shape or 2D spatial arrangement of the constituent PNAs. Consequently, the vast majority of reported multiresonant PNAs relying on in-plane or core-shell geometric engineering are unsuitable for hybrid integration with other types of optical or electronic nanodevices with predefined footprint geometries.[22] Along this direction, there are two key aspects to consider: fabrication and design degrees of freedom to achieve spectral tunability for multiresonant nanoantennas. For fabrication, a high-throughput CMOS-compatible fabrication technique is crucial to enable scalable fabrication for the widespread use of integrated hybrid platforms beyond the lab research purpose. For design degrees of freedoms, it remains to be determined whether a tunable multiresonant response can be attained when all characteristic design parameters (size, shape, and spacing) are predefined. These two considerations are especially critical for hybrid biomedical applications targeting cells for the following two reasons. First, the scalable nanofabrication can enable direct integration of fixed-size tunable PNAs with other types of nanodevices, such as micro-/nanoelectrodes, to achieve multimodal operations at the nano-bio interface.[23, 24] Second, minimizing nanodevice geometry variations at the nano-bio interface in an ordered array can promote controlled cellular responses to increase biomedical experiments' reproducibility.[25]

A suitable candidate to alleviate existing PNAs' design challenges can be sandwich-like nanolaminate metal-insulator-metal (MIM) nanostructures. By supporting a high-energy antibonding electric dipole (ED) mode and a low-energy bonding magnetic dipole (MD) mode, MIM nanostructures can serve as building blocks to construct metamaterials, metasurfaces, and composite nanoantennas.[26, 27] Since the nanolithography-based fabrication process typically involves using nanoholes as a deposition mask for physical vapor evaporation of alternating metal and dielectric layers, MIM nanostructures develop tapered sidewalls due to gradually closing nanohole as material accumulates at the top edges. In turn, the inversion symmetry at the surface is broken, opening rich hybridization schemes between vertically stacked nonidentical resonators. However, despite initial investigations on the plasmonic hybridization process in nanolaminate PNAs,[28-37] there is still a lack of experimental work to investigate the geometric tunability of multiresonant responses under strict size/footprint constraints for asymmetrical nanolaminate nanoantennas.

In this letter, we report that fixed-size tapered-shape nanolaminate nanoantennas (TNLNAs) can achieve a spectrally tunable double-resonant response by solely controlling the metal-to-insulator thickness ratio. We fabricated dense arrays of TNLNAs by electron-beam assisted evaporation of alternating Au and SiO_2 layers of varying thicknesses through nanohole array deposition masks. Extinction and dark-field scattering (DFS) spectroscopic measurements show that TNLNAs can support two widely tunable LSP modes with geometric dependence on the Au-to-SiO_2 thickness ratios. Furthermore, finite-difference time-domain (FDTD) simulations reveal that the geometry-dependent spectral tunability originates from modified resonant properties of elementary electric and magnetoelectric modes in their vertically stacked building blocks as well as their mutual coupling strength.

2.3 Results and Discussion

Figure 1(a) illustrates the soft-lithography nanofabrication process to create dense TNLNAs on glass substrates (see supplementary materials). Briefly, we employed the PEEL technique (photolithography, etching, e-beam evaporation, and lift-off)[38] to fabricate gold nanohole array (AuNHA) thin films with a nanohole diameter of ≈130 nm and film thickness of ≈120 nm to serve as a deposition mask to obtain TNLNAs. One wafer-scale AuNHA mask was cut into ~2cm x 2cm pieces and used in the deposition of three different TNLNAs with t/h conditions of t_{8nm}/h_{38nm}, t_{20nm}/h_{20nm}, and t_{28nm}/h_{8nm}, with the fixed total height of ~100 nm (Figure 1(b)).

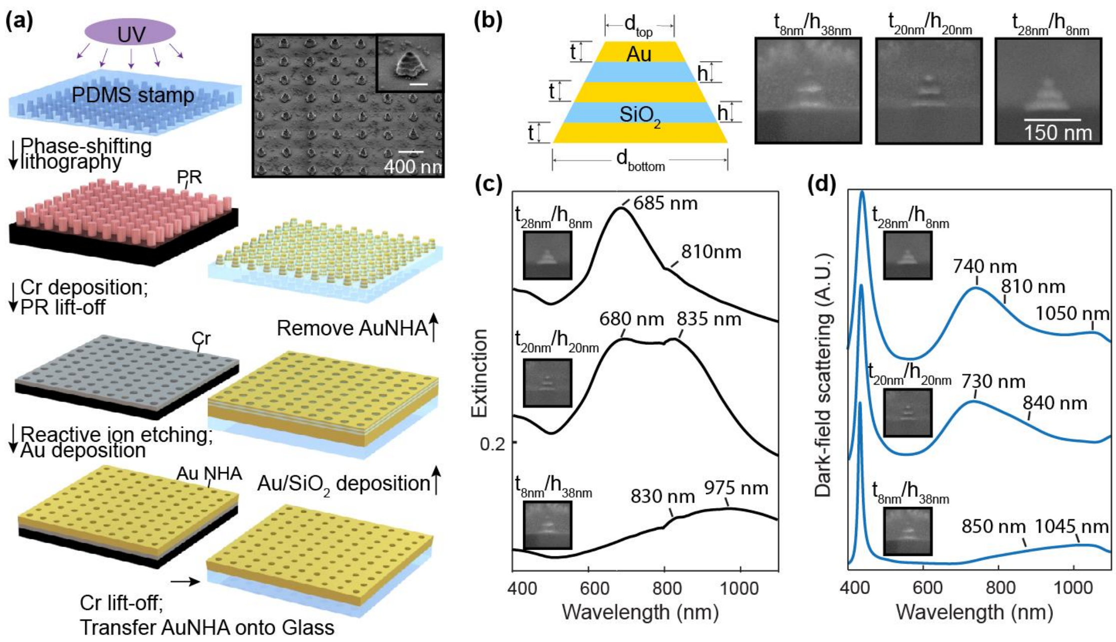

Figure 2.1 Fixed-size tapered-shape nanolaminate plasmonic nanoantennas (TNLNAs). (a) Scheme of the fabrication process and tilted-view scanning electron microscope (SEM) images of TNLNAs. Inset scale bar: 60 nm. (b) Cross-sectional schematic and SEM images of fixed-size TNLNAs with different Au-to-SiO_2 thickness ratios (t/h). (c) Measured normal-incidence extinction spectra and (d) dark-field scattering spectra for fixed-size TNLNAs with three different Au-to-SiO_2 thickness ratios (t/h: 8nm/38nm, 20nm/20nm, and 28nm/8nm).

To examine the far-field response of fixed-size TNLNAs with different t/h ratios, we performed extinction measurements (Figure 1(c)) using a UV-Vis-NIR spectrophotometer and dark-field scattering (DFS) measurements (Figure 1(d)) using a dark-field micro-reflectance setup (see methods). For the t_{8nm}/h_{38nm} TNLNAs, extinction shows an extensively broad peak feature at ≈ 975 nm with an additional resonant feature at ≈ 830 nm. DFS reveals a peak at ≈ 1045 nm and a shoulder feature at ≈ 850 nm. For the t_{20nm}/h_{20nm} TNLNAs, extinction shows two partially overlapped resonant features at ≈ 680 nm and ≈ 835 nm, and DFS reveals a broad asymmetrical scattering peak feature at ≈ 730 nm and a shoulder tucked at ≈ 840 nm. For the t_{28nm}/h_{8nm} TNLNAs, extinctions reveal a broad asymmetrical resonant feature at ≈ 685 nm with a gradually decaying lineshape towards the NIR region that envelops two features (≈ 810 nm and ≈ 1000 nm). DFS reveals a significant peak at ≈ 740 nm and a broad asymmetrical lineshape that indicates a feature at ≈ 810 nm and ≈ 1050 nm. Therefore, Figure 1(c)-(d) experimentally demonstrates that the fixed-size TNLNAs exhibit a double-resonant response with strong geometric dependence on the t/h ratios between the spectral range of 400 nm-1100 nm. Additionally, all three TNLNAs with different t/h show an absorption dip feature at a wavelength range less than 520 nm due to the Au interband electronic transition from the d band to the sp band.[39] Interestingly, all three TNLNAs exhibit a sharp emission peak at 440 nm in DFS measurements (Figure 1(d)), which originates from electron-hole pair radiative recombination following light absorption by the interband electronic transition in Au.[39, 40]

To connect far-field measurements with near-field optical properties, we performed FDTD simulations of the fixed-size TNLNAs with different t/h ratios (Figure 2).

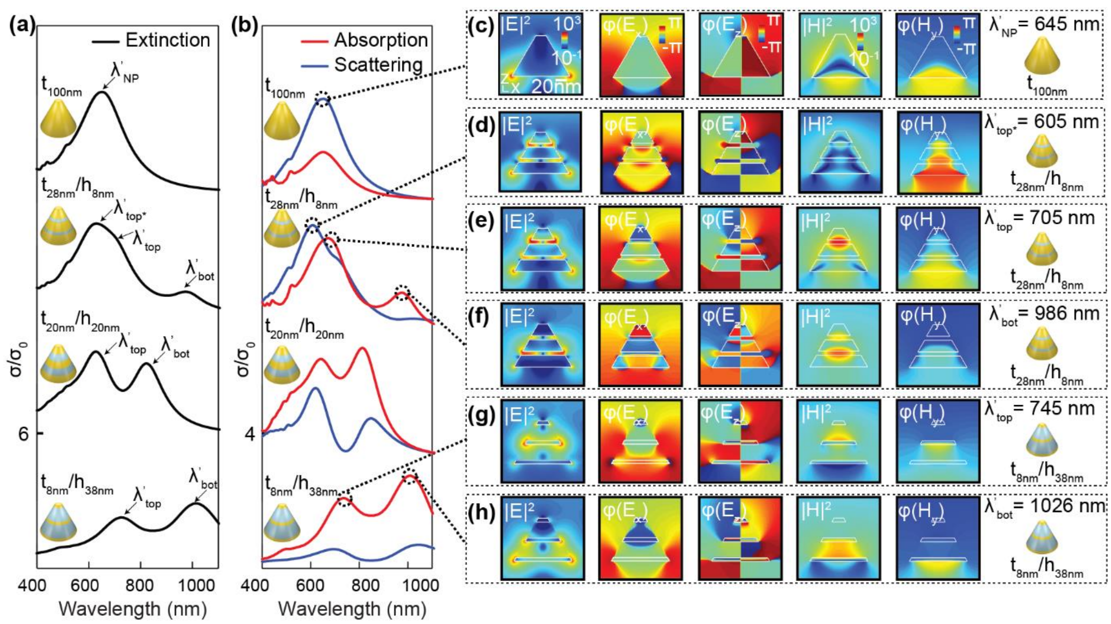

Figure 2.2 Calculated far-field and near-field optical properties. (a) FDTD-calculated extinction cross-section spectra and (b) absorption/scattering cross-section spectra for fixed-size TNLNAs with four different Au-to-SiO_2 thickness ratios (t_{100nm}, t_{8nm}/h_{38nm}, t_{20nm}/h_{20nm}, t_{28nm}/h_{8nm}). (c-h) FDTD-calculated distribution maps of $|E|^2$ and $|H|^2$ and phase distribution at resonant wavelength of (c) 645 nm, t_{100nm} (d) 605 nm (e) 705 nm (f) 986 nm, t_{28nm}/h_{8nm} (g) 745 nm (h) 1026 nm, t_{8nm}/h_{38nm}.

In the extreme case that h=0, TNLNAs turn into a tapered Au nanoparticle (AuNP) of the same size with a typical measured spectra as shown in Figure 3.

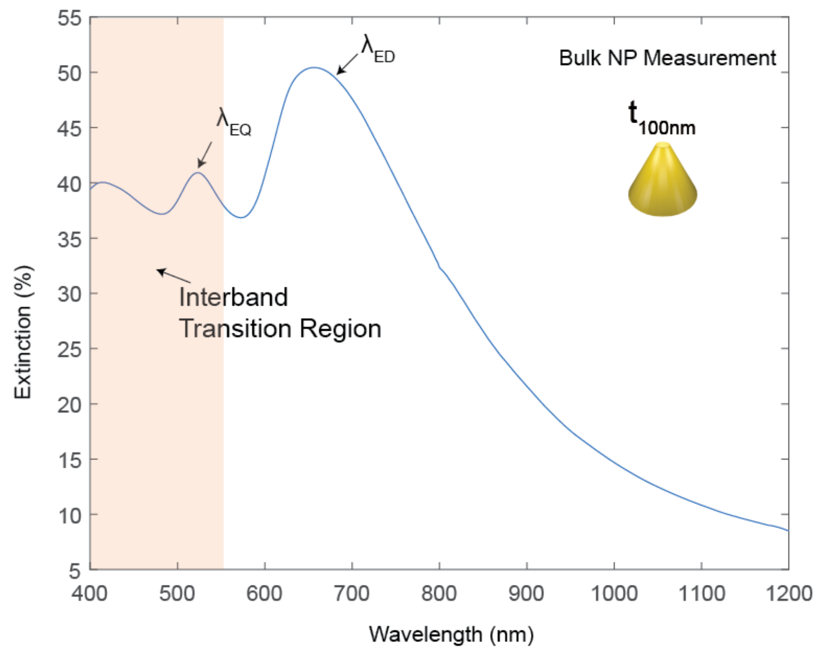

Figure 2.3 Measured normal-incidence extinction spectra of tapered-shape solid Au nanoparticle array with periodicity of 400 nm (AuNP)

There is a reasonably good match between the FDTD-calculated and measured spectral profiles for the AuNP and three TNLNAs samples. The measured resonant features show broader linewidths than their FDTD-calculated counterparts due to deposition-related broadening effects.[27] The calculated scattering spectra of TNLNAs do not show the observed emission peak at 440 nm because the FDTD package used for calculations is a linear system solver and thus does not capture the nonlinear photoluminescence from interband electronic transitions in Au.[41] Comparing the FDTD-calculated extinction, absorption, and scattering spectra of TNLNAs with different t/h and the Au NP of the same size reveals several distinct features. First, while the Au NP shows a single-resonant response with dominant scattering losses, the fixed-size TNLNAs show double-resonant responses with significantly increased absorption losses.

This observation indicates the TNLNAs' modes have different microscopic natures from the Au NP mode ($\lambda_{NP}^{'} = 645$ nm). Second, the double-resonant responses of fixed-size TNLNAs strongly depend on t/h, and the two modes' resonant wavelengths and spectral features evolve differently with t/h changes. Calculated extinction spectra (Fig. 2(a)) reveals that as t/h increases, the high-energy mode resonant wavelength first blueshifts from $\lambda_{top}^{'}(t_{8nm}/h_{38nm}) = 745\ nm$to $\lambda_{top}^{'}(t_{20nm}/h_{20nm}) = 637\ nm$ and then redshifts from $\lambda_{top}^{'}(t_{20nm}/h_{20nm})$ to $\lambda_{top}^{'}(t_{28nm}/h_{8nm}) = 705\ nm$. Simultaneously, the resonant wavelength of the low-energy mode first blueshifts from $\lambda_{bot}^{'}(t_{8nm}/h_{38nm}) = 1026\ nm$ to $\lambda_{bot}^{'}(t_{20nm}/h_{20nm}) = 806\ nm$ and then redshifts from $\lambda_{bot}^{'}(t_{20nm}/h_{20nm})$ to $\lambda_{bot}^{'}(t_{28nm}/h_{8nm}) = 986\ nm$. Therefore, by engineering t/h ratios, the low-energy mode can be spectrally tuned in a broader wavelength range ($\Delta\lambda_{bot}$≈200 nm) than the high-energy mode ($\Delta\lambda_{top}$≈100 nm). Third, the relative contributions from scattering and absorption to the total mode losses are different between the high-energy and low-energy modes and depend on t/h ratios in fixed-size TNLNAs. Lastly, for t_{28nm}/h_{8nm} TNLNAs, the broad high-energy extinction feature at

$680\ nm$ is due to interference between a superradiant mode's scattering peak at $605\ nm$ for λ'_{top*}(t_{28nm}/h_{8nm}) and a subradiant mode's absorption peak at $705\ nm$ for λ'_{top}(t_{28nm}/h_{8nm}).[11]
To investigate the microscopic nature behind the far-field spectral features of Au NPs and fixed-size TNLNAs, we plotted near-field distribution maps of field intensities ($|E|^2$ and $|H|^2$) and phases ($\varphi(E_x), \varphi(E_z)$, and $\varphi(H_y)$) for different modes as shown in Figure 2(c)-(h). For t_{100nm} Au NPs (Figure 2(c)), the resonant feature at λ'_{NP} manifests ED characteristics with a uniform $\varphi(E_x)$ within the Au NP, and it shows highly concentrated $|E|^2$ at the Au NP bottom edges while the top Au interface almost remains unexcited.

We can find an increased spectral and spatial overlap between the simultaneously excited gap modes for t_{28nm}/h_{8nm} to cause their interference, also reflected in the $\varphi(E_x)$ map (Figure 2(d)) with $\approx \pi$ change centralized in the top and bottom gap. The optical response shows dominant electric nature driven by the LSP at the bottom metal-substrate interface. The high-energy scattering peak at λ'_{top*}(t_{28nm}/h_{8nm}) exhibits dominant ED characteristics (Figure 2(d)). Next, the high-energy absorption peak at λ'_{top}(t_{28nm}/h_{8nm}) exhibits multipolar characteristics because of the aforementioned inference effects but shows overall dominant MD characteristics in the top MIM nanogap (Fig. 2(e)). Finally, the low-energy absorption peak at λ'_{bot}(t_{28nm}/h_{8nm}) shows electric and magnetic high-order multipolar characteristics with dominant MD characteristics in the bottom MIM nanogap (Figure 2(f)).

For low t/h, the high-energy resonant feature at λ'_{top}(t_{8nm}/h_{38nm}) exhibits (i) EQ characteristics with roughly out-of-phase $\varphi(E_x)$ distribution between the top two Au nanodisks, and (ii) MQ characteristics with out-of-phase $\varphi(H_y)$ between the two MIM nanogaps, yet the asymmetrical geometry gives rise to intense $|H|^2$ in the top MIM nanogap (Figure 2(g)). Comparatively, the low-energy resonant feature at λ'_{bot}(t_{8nm}/h_{38nm}) depicts (i) EQ characteristics with roughly out-of-phase $\varphi(E_x)$ distribution between the bottom and middle Au nanodisks, and (ii) MD characteristics with a higher $|H|^2$ in the bottom MIM nanogap and with in-phase $\varphi(H_y)$ in the two MIM nanogaps (Figure 2(h)), but the top MIM remains unexcited.

Unlike symmetric MIM building blocks supporting pure ED and MD modes, asymmetric TNLNAs can support magnetoelectric (ME) modes with bianisotropic responses due to the coupling between nonorthogonal electric and magnetic polarizabilities.[42] ME modes become prominent as the nanogap decreases (Figure 4(a)). The dominant elementary mode is dependent on t/h but based on the near-field characteristics, we can construct an energy level diagram for the extreme cases of t_{8nm}/h_{38nm} (Figure 4(b)) and t_{28nm}/h_{8nm} (Figure 4(c)).

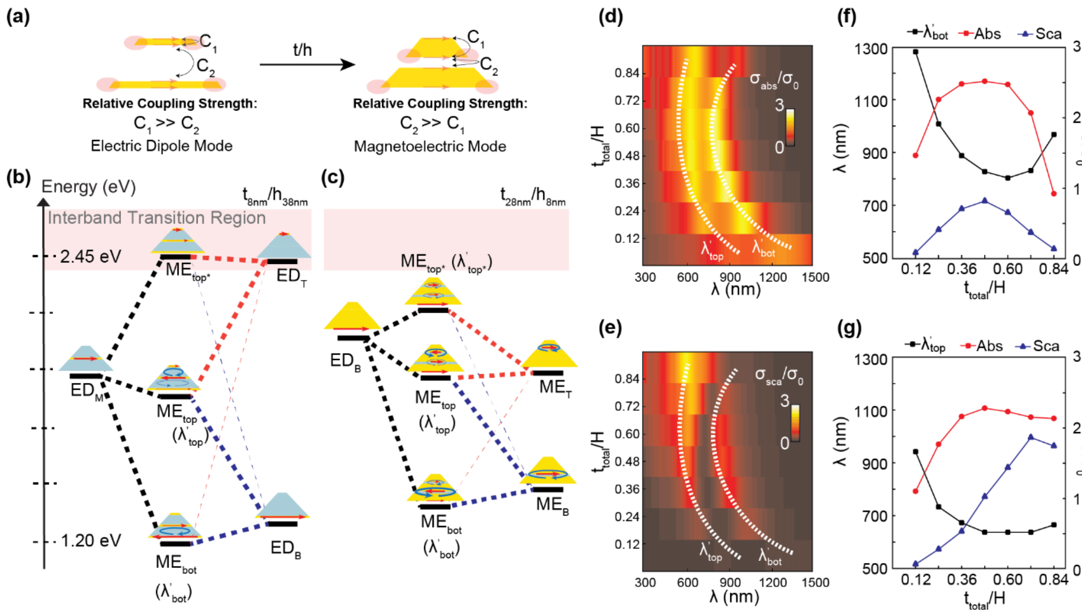

Figure 2.4 Microscopic and macroscopic trends of hybridized modes in TNLNAs. (a) Illustration of elementary mode coupling for thin and thick metal layers in MIM building blocks. (b, c) Hybridization energy level diagram for (b) t_{8nm}/h_{38nm} and (c) t_{28nm}/h_{8nm}. The red line-arrows and blue loop-arrows stand for the microscopic resonant sources with fundamental ED and MD characteristics. The arrow directions depict their relative phase relations, and the thickness stands for relative magnitude. (d, e) 2D color map as a function of total metal composition (t_{tot}/H) for normalized (d) absorption and (e) scattering cross-sections. (f, g) The dependence of the resonant wavelength and the peak absorption/scattering cross-sections on t_{tot}/H for (f) low-energy and (g) high-energy hybridized LSP modes.

For t_{8nm}/h_{38nm} TNLNAs with a low t/h ratio, each metal disk supports an elementary low-energy bonding ED mode and a high-energy antibonding EQ mode, as shown in Figure 5.[28] Due to high LSP coupling strength within thin metals, the EQ mode for the bottom, middle, and top disks blueshifts to the higher energy region (300-520 nm) with significant damping from interband electronic transitions. Therefore, the optical response is mediated by the coupling between the top (ED_T), middle (ED_M), and bottom (ED_B) elementary ED modes, as illustrated in the energy diagram in Figure 4(b). The middle ED_M mode can hybridize with the top ED_T mode to form a higher-energy ME mode ($ME_{top*}(\lambda'_{top*})$) with dominant ED characteristics, and with the bottom ED_B mode to form a high-energy ME mode ($ME_{top}(\lambda'_{top})$) with dominant MD characteristics in the top gap. The coupling between the middle ED_M mode with both ED_T and ED_B mode leads to a hybridized ME mode ($ME_{bot}(\lambda'_{bot})$) with dominant MD characteristics in the bottom gap. The coupling between individual metal layers, forming a top and bottom MIM building block, is shown in Figure 6. The optical response of the total MIMIM system is revealed to be a combination of the responses from individual top and bottom MIM building blocks.

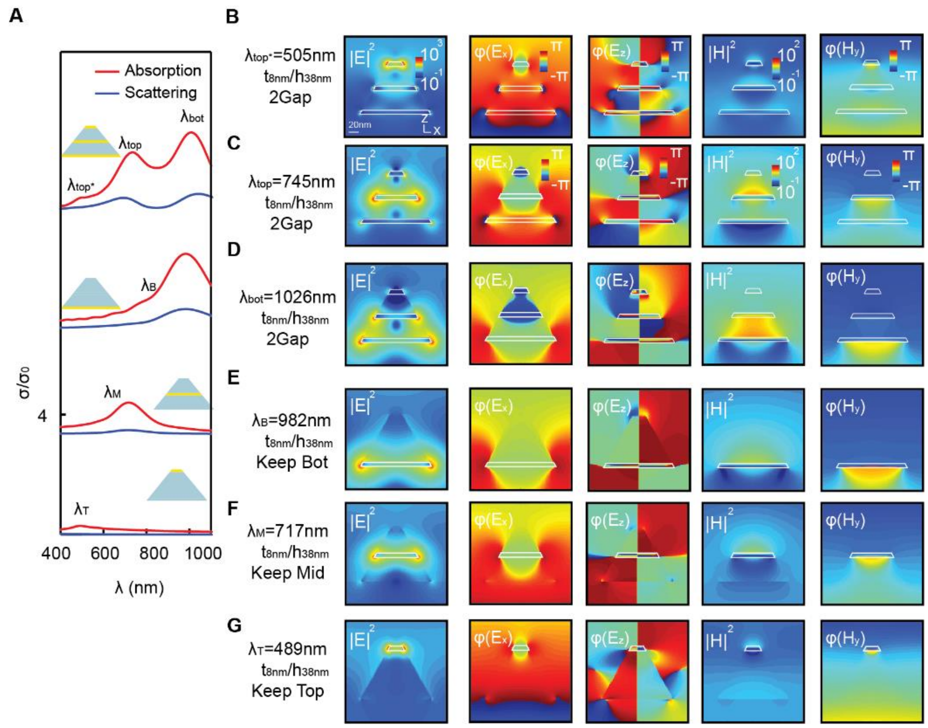

Figure 2.5 Far-field and near-field optical properties of fixed-size MIM nanolaminate plasmonic nanoantennas of t = 8 nm and h = 38 nm with different layer numbers as IMI building blocks. (A) FDTD-calculated spectra of normalized absorption and scattering cross-sections for Au-SiO_2-Au nanoantennas with 1, 2 gap systems. (B-F) FDTD-calculated distribution maps of $|E|^2$, $\phi(E_z)$, $\phi(E_x)$, $|H|^2$, and $\phi(H_y)$ of the magnetic related modes for fixed-size nanoantennas with different Au and SiO_2 layer numbers (B) Mode profile of 2-gap at λ_{top*}, (C) Mode profile of 2-gap at λ_{top}, (D) Mode of 2-gap at λ_{bot}, (E) Mode profile of 1-gap at λ_T, (F) Mode profile of 1-gap system at λ_{bot}, (G) Mode profile of 1-gap system at λ_{top*}.

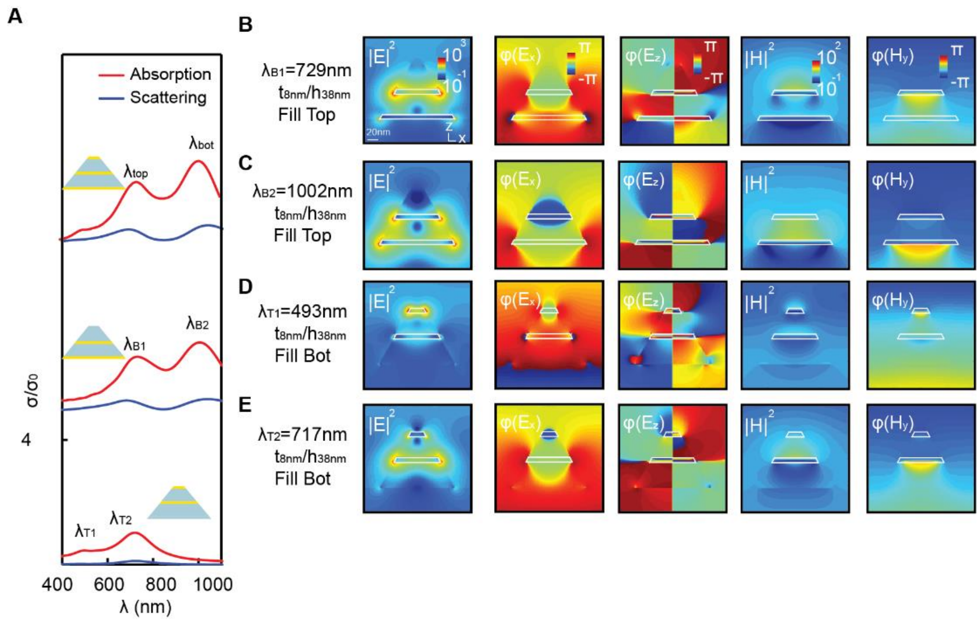

Figure 2.6 Far-field and near-field optical properties of fixed-size MIM nanolaminate plasmonic nanoantennas of single top and bottom gap MIM system. (A) FDTD-calculated spectra of normalized absorption and scattering cross-sections for Au-SiO_2-Au nanoantennas with whole, top, and bottom gap systems. (B-E) FDTD-calculated distribution maps of $|E|^2$, $\phi(E_z)$, $\phi(E_x)$, $|H|^2$, and $\phi(H_y)$ of the magnetic related modes for fixed-size nanoantennas with different Au and SiO_2 layer numbers (B) mode profile of bottom gap at λ_{B1}, (C) mode profile of bottom gap at λ_{B2}, (D) mode profile of top gap at λ_{T1}, (E) mode profile of bottom gap at λ_{B2}.

For t_{28nm}/h_{8nm}, the energy diagram in Figure 4(c) considers that the mode sustained by the bottom metal-substrate interface (ED_B) can couple with the elementary mode from the top (ME_T) and bottom (ME_B) MIM blocks as separate subsystems (see Figure 7).

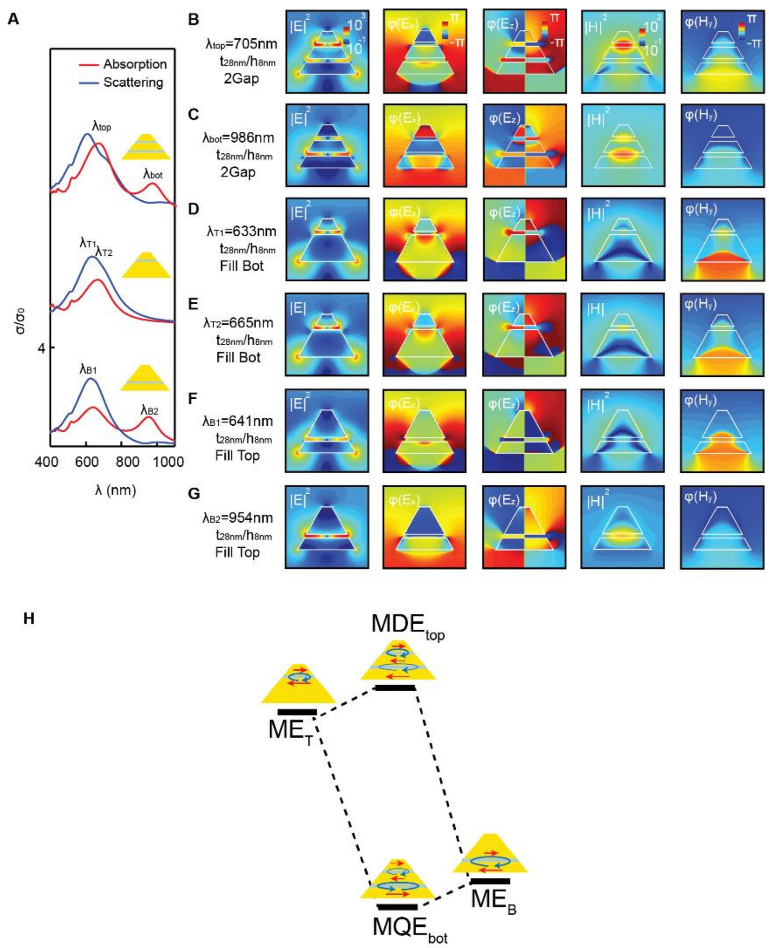

Figure 2.7 Far-field and near-field optical properties of fixed-size MIM nanolaminate plasmonic nanoantennas of single top and bottom gap MIM system. (A) FDTD-calculated spectra of normalized absorption and scattering cross-sections for Au-SiO_2-Au nanoantennas with whole, top, and bottom gap systems. (B-G) FDTD-calculated distribution maps of $|E|^2$, $\phi(E_z)$, $\phi(E_x)$, $|H|^2$, and $\phi(H_y)$ of the magnetic related modes for fixed-size nanoantennas with different Au and SiO_2 layer numbers (B) MH mode of 2-gap, (C) ML mode of 2-gap, (D) ME high energy mode of top 1-gap, (E) ME low energy mode of top 1-gap system, (F) ME high energy mode of the bottom 1-gap system, and (G) ME low energy mode of bottom 1-gap system, (H) Illustration of single-gap mode coupling in thick metal hybrid MIMIM system.

Because of its ME response with mutually coupled electric and magnetic polarizabilities, the ME_T mode in TNLNAs is nonorthogonal to the ED_B mode. Therefore, the ME_T and ED_B modes can further hybridize to generate a higher-energy mode ($ME_{top*}(\lambda'_{top*})$) with ED and MD characteristics and a high-energy mode ($ME_{top}(\lambda'_{top})$) with multipolar characteristics stemming from the EQ response, which is different from ideal cylindrical nanoantennas due to the off-resonant coupling between top and bottom interfaces as their diameters differ due to the tapered geometry. The spectral position and near-field characteristics of the multipolar mode involving the EQ response is shown in Figure 8. Furthermore, ME_B can hybridize with ED_B to form a low-energy mode ($ME_{bot}(\lambda'_{bot})$) with dominant MD characteristics.

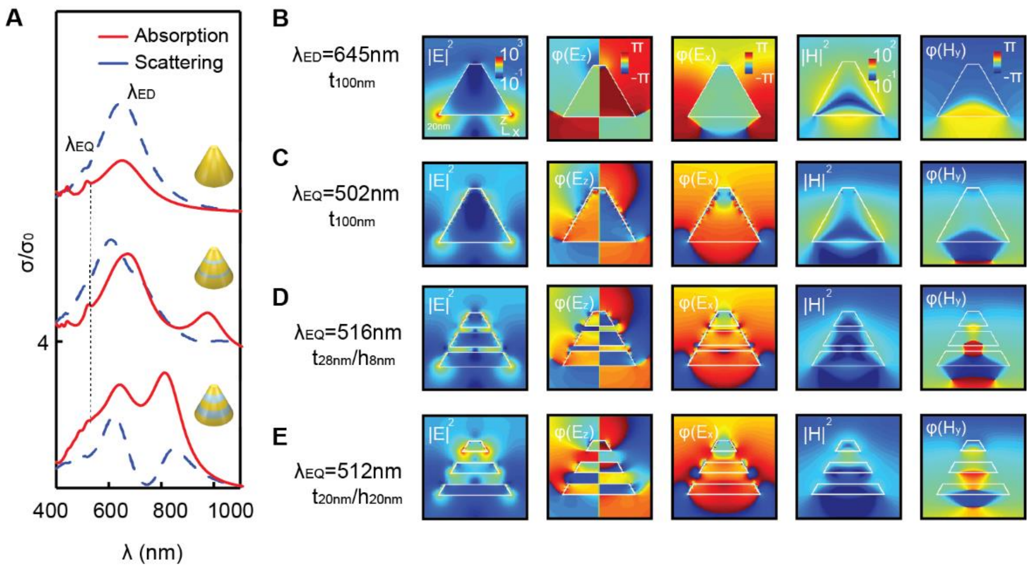

Figure 2.8 Far-field and near-field optical properties of fixed-size three-gap MIMIM nanolaminate plasmonic nanoantennas with different metal-to-insulator thickness ratios (t/h). (A) FDTD-calculated spectra of normalized absorption and scattering cross-sections for Au-SiO_2-Au-SiO_2-Au nanoantennas with a fixed size and different thicknesses for Au (t) and SiO_2 (h) layers. The total height (H) of Au-SiO_2-Au-SiO_2-Au nanoantennas is fixed as ~100 nm. (B-E) FDTD-calculated distribution maps of $|E|^2$, $\phi(E_z)$, $\phi(E_x)$, $|H|^2$, and $\phi(H_y)$ of the electric related modes for fixed-size Au-SiO_2-Au-SiO_2-Au nanoantennas with different thicknesses of Au and SiO_2 layers (B) ED mode of t = 100 nm, (C) EQ mode of t = 100 nm, (D) EQ mode of t = 28 nm, and h = 8 nm, (E) EQ mode of t = 20 nm and h = 20 nm.

To understand how absorption and scattering losses evolve with increasing metal composition in TNLNAs, we have plotted the 2D maps (Figure 4(d)-(e)) of absorption (σ_{abs}/σ_0) and scattering (σ_{sca}/σ_0) cross-sections as a function of the ratio between the total metal thickness (t_{tot}) and the fixed total height ($H = 100\ nm$), where $t_{tot} = 3t$ and $H = 3t + 2h$. The 2D map in Figure 3(d)-(e) shows the double-resonant response follows a parabolic-like shifting of λ'_{top} and λ'_{bot} from the NIR-Vis-NIR and shows that σ_{abs}/σ_0 and σ_{sca}/σ_0 appear to increase proportionally with t_{tot}/H for ME_{top}. For ME_{bot}, however, σ_{abs}/σ_0 and σ_{sca}/σ_0 appear to evolve similarly as ME_{top} but only up to a certain t_{tot}/H condition, which appears to correspond with the inflection point where λ'_{bot} reverses course from a blueshifting to a redshifting trend. Both magnetoelectric modes are dominated by the absorptive loss channel with significant ohmic losses in the form of thermal dissipation. Maximizing the absorption cross-section for nanoantennas is highly desirable for many biomedical applications based on photothermal processes, including plasmonic photothermal stimulation of electrogenic cells, plasmonic cell membrane optoporation for intracellular nanoprobe access or molecular cargo delivery, and photothermal tumor ablation for cancer therapy. On the other hand, for nanoantenna applications that prefer reduced absorption, possible solutions to minimize nonradiative losses for multiresonant TNLNAs include using post thermal annealing to reduce inelastic electron scattering at crystalline boundaries,[43] replacing gold with low loss plasmonic materials like titanium nitride,[44] or assembling nanoantennas in ordered arrays to couple with delocalized lattice modes.[45]

Upon closer inspection, the scatter plots of the absorption and scattering cross-sections (Figure 3(f)-(g)) reveal that as t_{tot}/H increases from 0.12 to 0.36 for ME_{bot},λ'_{bot} blueshifts from 1283nm to 890nm, accompanied by an increase in σ_{sca}/σ_0 from 0.08 to 0.82 and an increase in σ_{abs}/σ_0 from 1.46 to 2.52. As t_{tot}/H increases from 0.36 to 0.6, λ'_{bot} gradually blueshifts to 805 nm, but then rapidly redshifts to 970nm when t_{tot}/H increases beyond 0.60 to 0.84. Concurrently, the σ_{sca}/σ_0 for the ME_{bot} mode decreases to 0.14 and σ_{abs}/σ_0 decreases to 0.92 when t_{tot}/H increases from 0.48 to 0.84. As t_{tot}/H increases from 0.12 to 0.72 for the ME_{top} mode, λ'_{top} blueshifts from 946nm to 617nm and simultaneously, σ_{sca}/σ_0 increases from 0.06 to 1.86 and σ_{abs}/σ_0 increases from 1.09 to 2.28. As t_{tot}/H increases beyond 0.84, λ'_{top} redshifts to 669 nm and σ_{sca}/σ_0 decreases to 1.74 while σ_{abs}/σ_0 is maintained at 2.13. These observations suggest several critical points. First, the blueshift of λ'_{top} and λ'_{bot} as t_{tot}/H increases from 0.12 to 0.48 (low t/h) implies that the blueshifting of the elementary ED modes, which occurs as nanodisk t increases, dominates the overall spectral response. Second, there is a simultaneous competing redshift of the spectral response occurring as nanogap decreases, which begins to dominate as t_{tot}/H increases beyond 0.48 (high t/h), indicating a critical transition point where the increased splitting energy between ME_{bot} and ME_{top} mode results from the transition of a plasmonic system dominated by the ED mode of individual metallic nanodisks to one dominated by the elementary ME mode of individual insulator nanogaps. Lastly, the ME_{bot} mode has attributes of a dark (subradiant) mode of multipolar nature. It is typically challenging to be excited in in-plane plasmonic systems and requires breaking the in-plane geometric symmetry or employing oblique-angle illumination with retardation effects.[46] While the circular symmetry of isolated TNLNAs' shape leads to an EM response which is independent of the normal incident light polarization,[34] the out-of-plane vertical stacking of building blocks offers a unique avenue to excite and spectrally tune the dark multipolar modes through the out-of-plane mode hybridization without altering the overall size and footprint.[46]

2.4 Conclusion

In conclusion, fixed-size tapered-shape nanolaminate nanoantennas (TNLNAs) composed of vertically stacked MIM plasmonic building blocks can exhibit tunable double-resonant optical responses by out-of-plane engineering of the metal-to-insulator thickness ratio controlled by thin-film deposition. Numerical studies reveal that TNLNAs support two magnetoelectric modes from the hybridization of elementary modes in vertically stacked MIM building blocks. Besides being spatially overlapped, the two magnetoelectric modes show large resonant optical cross-sections, significant field enhancements, and broad spectral tunability in the visible-to-near-infrared regime. Hence, spectrally tunable double-resonant TNLNAs are suitable for direct integration with other nanodevices of a predefined footprint for multimodal operations, especially in nano-bio interfacing applications requiring constrained structural design and minimized geometric variations.

2.5 Methods

2.5.1 Nano-Fabrication of Nanolaminate Plasmonic Nanoantennas

Step 1: We do phase-shifting lithography using PDMS and MA6 contact lithography tools to expose negative photoresist.
Step 2: After developing the photoresist, we deposit a thin sheet of chrome and lift-off photoresist pillars, leaving a thin chrome hole array on flat silicon. (Note: the chrome layer serves as a sacrificial lift-off layer).
Step 3: After etching the silicon wafer through the Chrome holes, we deposit gold. (Note: the nanohole diameter depends on shadow angle from directional electron beam deposition).
Step 4: We place the wafer in chrome etchant to lift off the gold nanohole array and then transferred it in DI water solution - a glass substrate is used to "scoop" the Au Nanohole Array (AuNHA) (Note: the glass substrate is cleaned using oxygen plasma).
Step 5: After transferring Au NHA, we deposit the alternating layers of Au and SiO_2 (Ti (0.7nm) used as an adhesion layer).
Step 6: We remove Au NHA with scotch tape, thus expose a periodic gold nanoantenna array.
Note: lattice periodicity of NHA used for deposition is 400 nm.

2.5.2 Spectroscopic Experimental Set-Up

We obtained dark-field scattering spectra using a 50x objective with a NA of 0.55 with an acceptance half-angle of $\alpha = 33°$ as shown in Fig. S1. For clarity, we smoothed both TNLNAs and reference light source scattering spectra data using a moving average filter and normalized the scattering signal as defined in equation (S1)[47]

$$I_{scat}(\lambda) = \frac{I_{TNLNAs} - I_{dark}}{I_{halogen} - I_{dark}} \qquad (S1)$$

For extinction spectra, the extinction is defined as $1 - |T|^2$ with T being the amplitude transmission coefficient, we obtained by measuring the transmission of TNLNAs with a bright field halogen light source with a normalization scheme of the same form in equation (S1). The spectrometer's grating switches at the spectral position of 800 nm, which results in a slight change in signal and can be stitched together.

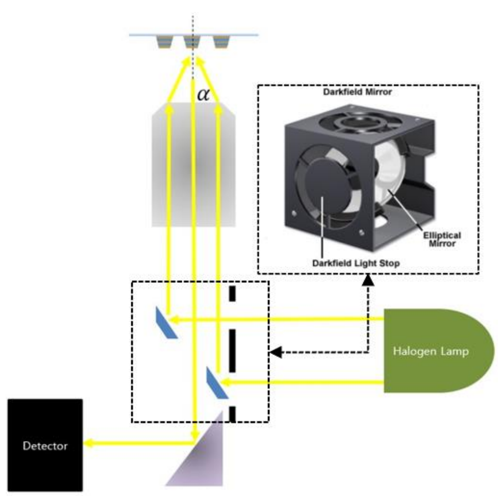

Figure 2.9 Reflective Dark-Field Scattering Configuration

2.5.3 Finite Difference Time Domain (FDTD) Simulation Condition

All numerical simulations are supported by the three-dimensional finite-difference-time-domain (FDTD) method by commercial software. We have used a total-field-scattered-field (TFSF) source with normal incidence from the top in all simulations. All the metal and the dielectric materials are Au (Johnson and Christy) and SiO2 (n=1.5), respectively, with air background (n=1.0) and no substrate. The mesh size for x,y-directions used is 2nm, and for z-direction, it's 1 nm. 1 nm Ti is inserted between each layer, and 1 nm Cr is inserted between the substrate and bottom metal layer. The Source is TFSF with TEM incidence, and two box monitors are placed in the nanostructure region. The one place outside of the TFSF calculates the total scattering cross-section, while the one inside the TFSF calculates the absorption cross-section. The backscattering cross-section is calculated based on the power flow through the top side of the scattering box. A 2D monitor is placed inside the TFSF source and below to the nanolaminated structure to calculate the transmission (includes forward scattering). It must be noted simulations are constructed for a single unit while measurements account for ensemble nanoantenna response.

2.5.4. Near-Field Characteristics

The high-energy scattering peak at λ'_{top*}(t_{28nm}/h_{8nm}) exhibits (*i*) ED characteristics with a roughly in-phase $\varphi(E_x)$ distribution in the middle and bottom Au nanodisks, and (*ii*) MD characteristics with a minimal $\varphi(H_y)$ difference between the two MIM nanogaps (Fig. 2(d)). Next, the high-energy absorption peak at λ'_{top}(t_{28nm}/h_{8nm}) exhibits (*i*) electric quadrupole (EQ) characteristics with out-of-phase $\varphi(E_x)$ distribution between the top and the other two Au nanodisks, and (*ii*) MD characteristics with an enhanced $|H|^2$ in the top MIM nanogap (Fig. 2(e)). Finally, the low-energy absorption peak at λ'_{bot}(t_{28nm}/h_{8nm}) shows (*i*) electric high-order multipolar characteristics with roughly out-of-phase $\varphi(E_x)$ distributions alternating among the center portion of the top, middle, and bottom Au nanodisks, and (*ii*) magnetic quadrupole (MQ) characteristics with a higher $|H|^2$ in the bottom gap (Fig. 2(f)).

Chapter 3. Scalable 2-Tier Protruding Micro-/Nanooptoelectrode Arrays with Hybrid Optical-Electrical Modalities by Hierarchical Modular Design

(This chapter has been published in Nanoscale.[48] This paper is published by the Royal Society of Chemistry.)

3.1 Abstract

In situ spatiotemporal characterization of correlated bioelectrical and biochemical processes in living multicellular systems remains a formidable challenge but can offer crucial opportunities in biology and medicine. A promising approach is to develop bio-interfaced multifunctional micro-/nano-sensor arrays with complementary biophotonic-bioelectronic modalities and biomimetic topology to achieve combined bioelectrical and biochemical detection and tight device-cell coupling. However, a system-level engineering strategy is still missing to create multifunctional micro-/nano-sensor arrays that meet the multifaceted design requirements for *in situ* spatiotemporal characterizations of living systems. Here, we demonstrate a hierarchical modular design and fabrication approach to develop scalable two-tier protruding micro-/nano-optoelectrode arrays that extend the design space of biomimetic micro-/nano-pillar topology, plasmonic nanoantenna-based biophotonic function in surface-enhanced Raman spectroscopy (SERS), and micro-/nano-electrode-based bioelectronics function in electrochemical impedance spectroscopy (EIS). Notably, two-tier protruding micro-/nano-optoelectrode arrays composed of nanolaminate nanoantenna arrays on top of micropillar electrode arrays can support plasmonic nanocavity modes with high SERS enhancement factors ($\approx 10^6$) and large surface-to-volume ratio with significantly reduced interfacial impedance in EIS measurements. We envision that scalable two-tier protruding micro-/nano-optoelectrode arrays can potentially serve as bio-interfaced multifunctional micro-/nano-sensor arrays for *in situ* correlated spatiotemporal bioelectrical-biochemical measurements of living multicellular systems such as neuronal network cultures, cancerous organoids, and microbial biofilms.

3.2 Introduction

Living multicellular systems, ranging from neuronal networks to cancerous tumors and microbial biofilms, feature dynamic, heterogeneous, and adaptive biological activities coordinated by cellular interactions through various bioelectrical and biochemical signaling pathways.[49] Unfortunately, conventional bioanalysis methods based on single-modal end-point measurements have difficulty resolving spatiotemporal correlations between bioelectrical and biochemical processes in living systems, impeding the understanding of complex biological activities from a holistic systems-biology approach. Therefore, it is desirable to establish new methods for multimodal spatiotemporal measurements of multiple correlated bioelectrical and biochemical processes across multicellular systems.[50] A potential approach is to develop bio-interfaced multifunctional micro-/nano-sensor arrays with complementary bioelectronic-biophotonic detection modalities to allow multimodal spatiotemporal measurements of living multicellular systems.

With the increasing availability of micro-/nano-fabrication tools, the past two decades have seen significant advances in micro-/nano-scale bioelectronic and biophotonic devices for biosensing and bioanalysis of living systems.[2, 23, 24, 51-64] For example, micro-/nano-electrode arrays have demonstrated great utility for spatiotemporal measurements of bioelectrical activities in networks of electrogenic cells, including neurons and cardiac myocytes.[57-61] Notably, micro-/nano-electrodes with protruding biomimetic topologies, such as micro-/nanopillar structures, can elicit spontaneous cell engulfment behaviors for a tight device-cell coupling to achieve intracellular-like electrical recording of membrane potentials in electrogenic cells.[62, 63] On the other hand, plasmonic nanoantennas made of noble metal nanostructures can concentrate light at the nanoscale to enable surface-enhanced Raman spectroscopy (SERS) biochemical analyses of living cells with molecular vibrational fingerprint information.[2, 64] Despite the apparent benefits, there is little research in developing micro-/nano-optoelectrodes (*i.e.*, combined micro-/nano-electrode and nanoantenna devices) in large arrays for multimodal spatiotemporal measurements of bioelectrical and biochemical information in living systems. In particular, there is a lack of a system-level modular design approach to create bio-interfaced micro-/nano-optoelectrode arrays with optimized hybrid device properties for achieving multimodal bioelectrical recording, SERS biochemical analyses, and tight nanodevice-cell coupling by biomimetic design. A significant challenge limiting the modular design space resides in the difficulty of patterning nanoscale features on non-planar large-scale (cm scale) areas using conventional nanofabrication techniques such as electron-beam lithography or ion-beam milling. Alternatively, light can be used to pattern both micro- and nanoscale features, opening opportunities for a modular design approach. For example, modern additive fabrication techniques based on stereolithography[65] and 2-photon polymerization[66] have enabled rapid prototyping of complex 3D micro-/nano-scale features, which potentially can be used to create next-generation micro-/nanostructured optical, electrical, and mechanical systems. Standard mask/maskless photolithography-based fabrication techniques have also been employed to create 3D micro-scale features with sizes constrained by the diffraction limit and penetration depth of UV light in photoresists. Advanced photolithography techniques using phase-shifting interference effects can directly generate nano-patterns.[67, 68] Despite significant efforts, it remains challenging for existing light-based fabrication techniques to achieve modularized integration of micro-/nano-scale building blocks with different constituent materials.

In this work, we devise a hierarchical modular design and fabrication methodology to integrate multiresonant plasmonic nanoantenna arrays on top of micropillar electrode arrays, producing a general class of two-tier protruding micro-/nano-optoelectrode arrays, which feature biomimetic topology and complementary biophotonic-bioelectronic modalities for bioelectrical recording and surface-enhanced Raman spectroscopy (SERS) biochemical detection. The method involves a multilayer lift-off process to create three-dimensional (3D) protruding structures with electrical interconnects and soft interference lithography to create nanohole array deposition masks for patterning metallic-dielectric nanoscale features on hierarchical surfaces. The combination of nanolaminate nanoantennas and conductive micropillars elicits unique optical and electrical characteristics that can be exploited with further optimization and experimentation. For optical characteristics, the micro-reflectance of a single micro-/nano-optoelectrode shows a double-resonant optical response in the visible/near-infrared window because of the excitation of multiple hybridized plasmonic modes. Stokes inelastic scattering signals from a bound thiol molecule enjoy a six-order of magnitude enhancement due to the nanoantenna's intense near-field enhancement and spectral mode overlap at the laser excitation wavelength. The calculated far-field and near-field optical properties using the finite-difference time-domain (FDTD) method reveal that the measured high SERS enhancement factors ($\approx 10^6$) result from intense localized optical fields due to constructive near-field interference of multipolar plasmonic modes in nanolaminate nanoantennas with their induced image in the metallic mirror ground plane. For electrical characteristics in 1× phosphate-buffered saline, electrochemical impedance measurements show one order of magnitude reduction in the electrochemical impedance due to an increase in electrochemically active surface area compared to a planar electrode. Furthermore, cyclic voltammograms reveal large charging currents for micro-/nano-optoelectrodes compared to planar electrodes due to the more extensive electric double layer (EDL) at the interface between the conductive 3D electrode and aqueous electrolyte, potentially benefiting other applications such as supercapacitors, fuel cells, electroporation devices, and dielectrophoretic devices.[69]

3.3 Results and Discussion

3.3.1 Top-down Modular Fabrication Procedure

Figure 3.1 illustrates the procedure of fabricating two-tier protruding micro-/nano-optoelectrode arrays in a modularized, scalable, and complementary metal-oxide-semiconductor (CMOS) compatible manufacturing process. A combination of microscale photolithography, phase-shifting lithography, and thin-film physical vapor deposition (PVD) enables the control of the geometry and material processing parameters for micropillars, microelectrodes, and nanoantennas.

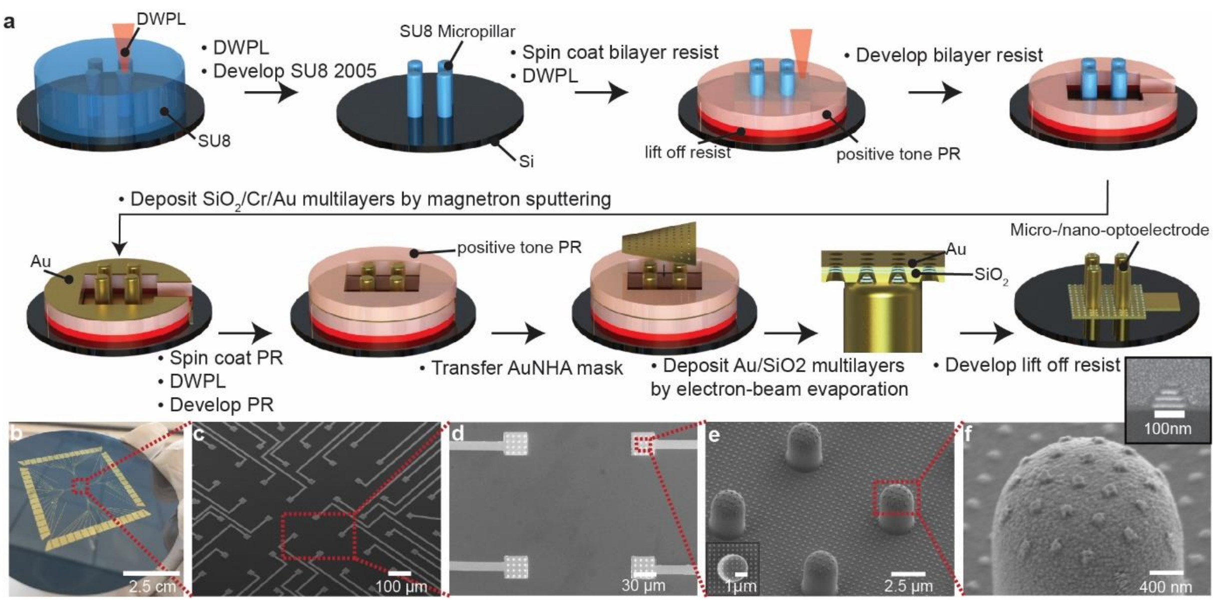

Figure 3.1 Wafer-scale two-tier protruding micro-/nano-optoelectrode arrays by hierarchical modular design. (a) Schematic illustration of the fabrication process. DWPL: direct write photolithography, PR: photoresist (b) Camera image of the wafer-scale sample. (c) Perspective SEM image of microelectrode pad arrays (pad size: 30 × 30 mm^2) with contact lines. (d) The top-down SEM image shows that each microelectrode pad consists of a 4 × 4 array of protruding micropillar electrodes (diameter ≈ 2.5 mm, height ≈ 5 mm). (e) The perspective and (f) magnified SEM images show that each protruding micropillar electrode consists of Au/SiO_2/Au/SiO_2/Au nanolaminate nanoantenna arrays on the top. The inset of Figure 3.1e illustrates the cross-sectional SEM image of a nanolaminate nanoantenna.

The nanofabrication procedure begins with the patterning of a superlattice array of polymeric (SU-8) micropillars (diameter ≈ 2.5 mm, height ≈ 5 mm) on a silicon wafer using direct-write photolithography (DWPL). Alignment markers ensure precise overlap between micropillars and the multi-electrode (MEA) array pattern. Second, we define the microelectrode, contact lines, and contact pads by spin-coating and DWPL of a bilayer resist stack consisting of a nominally 1.3 mm thick positive-tone photoresist (PR) and a 500 nm thick lift-off resist on top of the protruding micropillar MEA. Subsequently, an undercut was developed in the bilayer photoresist stack for thin-film deposition (**Figure 3.2**).

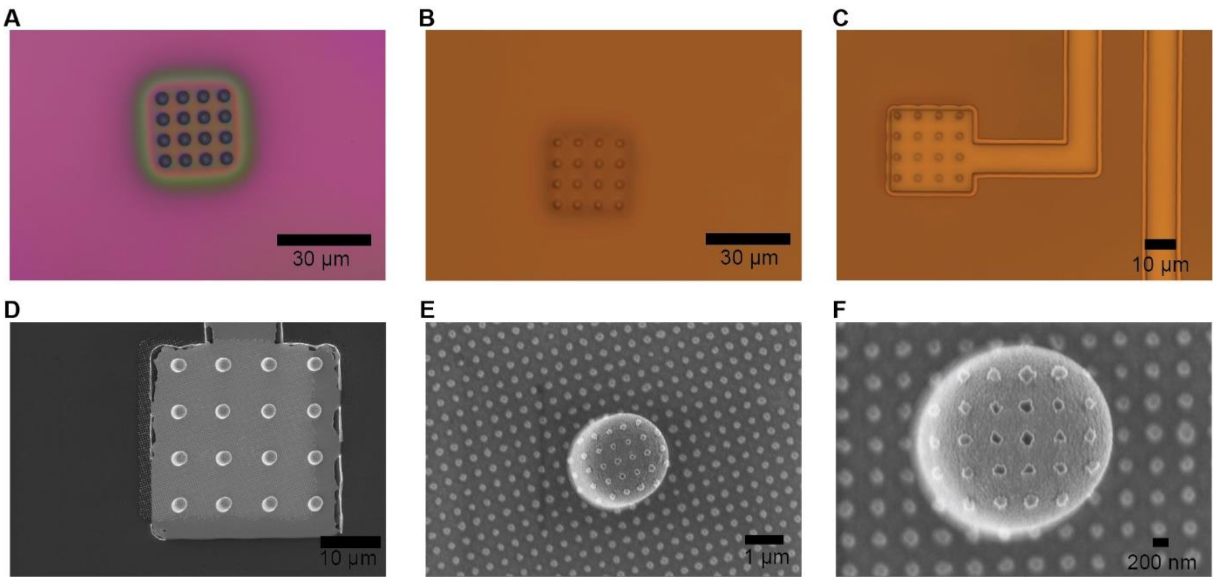

Figure 3.2 Intermediate fabrication steps and final structure imaged with optical microscope and SEM. Optical images show (A) Lift-off resist (LOR) around pillar array, (B) PR-LOR bilayer resist stack, (C) development of PR and undercut of LOR revealing electrodes and contact lines. SEM images show (D) electrode with protruding out-of-plane micropillars and nanoantenna array, (E) single micropillar with nanoantenna array at the base, (F) shape variation of nanoantennas on top of the micropillar.

Third, we deposited approximately ≈30 nm of SiO_2, ≈10 nm of Cr, and ≈100 nm of Au by magnetron sputtering PVD to achieve conformal sidewall coating of micropillars, structurally anchoring the micropillars on each of the microelectrodes with corresponding contact lines and pads for the electrical interface. Fourth, spin-coating and DWPL of an additional PR layer enabled us to mask the entire chip except for the 64 square microelectrode regions, selectively constraining the regions for nanoscale pattern transfer during the PVD process. Next, we transferred onto the chip a precut 1 cm × 1 cm Au film perforated with an ordered nanohole array (AuNHA), which was prefabricated using soft interference lithography[38] with a resultant nominal hole diameter of ≈130 nm and periodicity of ≈ 400 nm (see methods for AuNHA fabrication details). For the transfer process, we lifted off the AuNHA from its carrier substrate, then transferred and resuspended the AuNHA thin-film in a large water-filled glass dish, enabling us to submerge a glass slide (75 mm x 26 mm) and remove the thin-film in a scooping manner. Prior oxygen plasma treatment of the microscope slide resulted in a hydrophilic surface and improved the scooping process. The AuNHA was subsequently transferred onto the micropillars by positioning one edge of the glass slide directly over the center of the wafer with a slight angle

and simultaneously using a plastic pipette to provide a stream of water, dragging the thin film from the glass slide onto the wafer. The remaining water underneath the AuNHA was left to evaporate at room temperature. Following the AuNHA transfer, we deposited alternating layers of Au (nominal thickness = 12 nm) and SiO_2 (nominal thickness = 9 nm) by electron-beam evaporation PVD without substrate rotation to maintain a direct line-of-sight between the sample and crucible. We included Cr (thickness = 1 nm) as an adhesion layer with Au micropillars and Ti (thickness = 0.7 nm) as the interfacial adhesion layers between Au and SiO_2. A 1-methyl-2-pyrrolidone (NMP) based solvent stripper is used to complete the lift-off process and reveal metalized MEA pattern on the silicon wafer. A camera image shows the footprint of the final device, which covers an area of 5 cm × 5 cm on a three-inch silicon wafer (**Figure 3.1b**).
We characterize the structural properties at different length scales using micrographs from an optical microscope and scanning electron microscope (SEM). The SEM micrograph in **Figure 3.1c** shows a square array of 8 × 8 uniformly patterned microelectrode pads (size: 30 µm × 30 µm, spacing: 100 µm) with contact lines. For a side-by-side comparison, both the planar and 3D optoelectrodes were made using the same 2D mask layout and bilayer lift-off process, ensuring the same areas and thicknesses of the metal layers in the experiments. Before commencing with the fabrication process of both samples, we ensured accurate sputtering thickness control of SiO_2, Cr, and Au by depositing each material separately on the silicon wafers and measuring the thickness using an ellipsometer to calibrate the deposition rates accurately. A top-down SEM image shows a 4 × 4 array of micropillars on each microelectrode pad (**Figure 3.1d**). The micropillar height is controlled by the spin-coating thickness of the SU-8 resist, which was nominally 5 µm in our procedure. After several development cycles for different resists in the fabrication process, we observed a decrease in pillar height (≈ 4 µm) with rounded top edges. Magnified SEM images of a single electrode pad reveal highly ordered nanoantenna arrays on the bottom microelectrode pad surface and the top of the protruding micropillars. The inset in **Figure 3.1e** shows a top-down view of a single micropillar. To ensure micropillar structural and chemical integrity, we promote complete SU-8 polymer resist cross-linking by baking the chip on a hot plate at 180 ˚C for 45 min. A closer look at the micropillar top reveals the nanolaminate nanoantennas conformally covering the top surface of the micropillars (**Figure 3.1f**). Lastly, a cross-sectional SEM image obtained by focused ion milling (**Figure 3.1f inset)** shows the nanolaminate composition of a single nanoantenna with $Au/SiO_2/Au/SiO_2/Au$ multi-layers and a tapered shape due to the shadowing effect of accumulated material around the nanoholes, altering the line-of-sight electron-beam PVD through the AuNHA mask.[1, 27]

3.3.2. Optical Properties and SERS Performance

To characterize the passive optical response of the micro-/nano-optoelectrodes, we used a commercial confocal microscope equipped with a spectrometer in a dual-source configuration to obtain (*i*) single-point micro-reflectance spectral response and (*ii*) average SERS sensing performance and two-dimensional Raman scattering spatial distribution maps from a two-dimensional (2D) slice intersecting the micropillar domes (**Figure 3.3**).

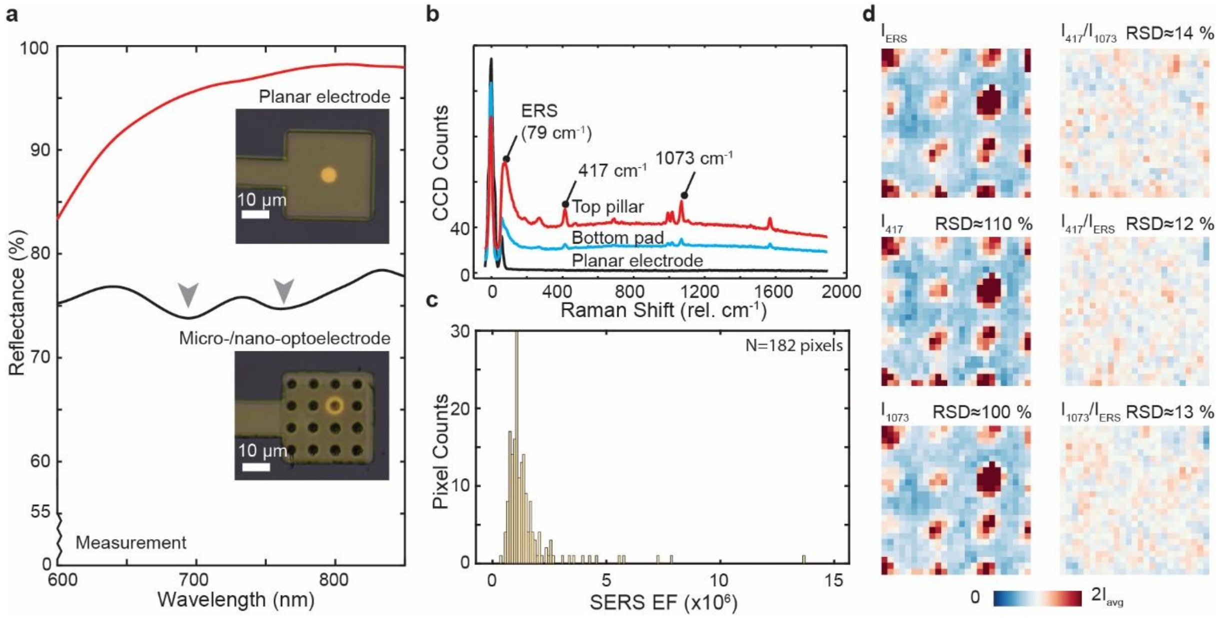

Figure 3.3 Optical properties and SERS performance. (a) Measured micro-reflectance spectra of the micro-/nano-optoelectrodes and the planar electrode. (b) Measured Raman spectra of BZT molecules from the top and bottom surface of micro-/nano-optoelectrodes and the planar electrode (averaged from 625 total pixels). For clarity, the spectra are offset in the *y*-axis by 10 charge-coupled device (CCD) counts. (c) Histogram of Raman signal intensities and the corresponding SERS enhancement factor (EF) for 1073 cm^{-1} BZT peak from the top surface of micro-/nano-optoelectrodes. (d) 2D Raman mapping images of I_{ERS} at 79 cm^{-1}, I_{417} at 417 cm^{-1}, I_{1073} at 1073 cm^{-1}, I_{417}/I_{ERS}, I_{1073}/I_{ERS}, and I_{417}/I_{1073} with the scale normalized between 0 and $2I_{avg}$.

The reflectance from a planar electrode shows the typical flat metal film response, increasing gradually to ≈ 97 % from 600 nm to 850 nm. In contrast, for the same wavelength span, the reflectance from a single micro-/nano-optoelectrode micropillar exhibits a broadband reduction in intensity by up to ≈ 20 % at 850 nm and spectral dip features at ≈ 690 nm and ≈ 760 nm, manifesting the double-resonant response of plasmonic nanolaminate nanoantennas. For SERS measurements, we disabled the white-light source port used for micro-reflectance measurements and enabled the diode laser source with a wavelength of 785 nm and a nominal average power of 1 mW. Both the planar electrode and micro-/nano-optoelectrode were coated with a non-resonant Raman probe, benzothiazole (BZT), to form a bound monolayer on Au surfaces. The BZT molecule bound to the gold surface on micro-/nano-optoelectrodes exhibits distinct vibrational Raman scattering signatures at 417 cm^{-1}, 1021 cm^{-1}, 1073 cm^{-1}, 1569 cm^{-1}, allowing us to estimate the SERS enhancement factor (EF) and spatial distribution.[70] The average SERS response of a sputtered planar electrode shows a low wave-number pseudo peak attributed to electronic Raman scattering (ERS) due to the relaxation of momentum conservation by momentum transfer from microscopic surface roughness.[71] However, no discernable Raman scattering signatures are present in the spectra due to the absence of strong local field enhancement to increase the vibrational transition rates of the BZT molecules (**Figure 3.3b**). By separating the pixels corresponding to the top pillar plane and bottom pad surfaces of the micro-/nano-optoelectrode array, we find that the overall BZT signal from the top surface is one order of magnitude larger than the BZT signal from the bottom surface, which originates from the effects of off-focus excitation beyond the focal depth and the partially partitioned signal collection from the pinhole in the confocal configuration, allowing normal-incidence reflected light from the background. Beyond Raman scattering signals, we can see an inverse relationship in the linear Rayleigh and nonlinear electronic Raman scattering signals, indicating the depletion of the incident laser energy and reconversion through plasmon-enhanced nonlinear decay channels, evidenced by a larger ERS signal for the in-focus top micropillar regions. Furthermore, the linear Rayleigh scattering signal conveys the reflective (optical path length) differences of the two-tiered micro-/nano-optoelectrode, allowing for the segmentation of the micropillar tops from the bottom pad. Specifically, the average Rayleigh scattering peak was used as a threshold to distinguish between the corresponding top pillar and bottom pad pixels in the 2D Raman maps (**Figure 3.4**).

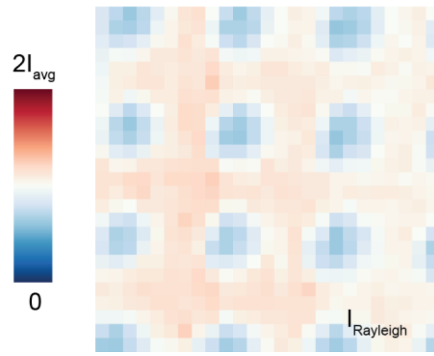

Figure 3.4 Confocal Raman image of Rayleigh scattering peak (0 cm^{-1}).

Using the average SERS signal from the peak at 1073 cm^{-1} for the top pillar regions, we estimate the SERS EF distribution in the histogram shown in **Figure 3.3c** with a mean EF of ≈ (1.56 ± 1.75) ×10^6. The experimental statistical uncertainty is given by one standard deviation above and below the mean value. The source of the uncertainty in the measured BZT signal and subsequently the enhancement factor can arise from (i) variations of BZT molecular orientation due to the curved surface of micropillar tops, (ii) possible surface area competing effects of residual resist, preventing a uniform self-assembled BZT monolayer coverage, and (iii) differences between the focusing plane and micropillar domes in the 2D area scans. Notably, the scanning procedure entailed focusing on one micropillar dome and maximizing the ERS signal to establish a fixed vertical (z) position of the focal plane for the entire scan, and the 2D area bounds were set using software controls that communicated with an automated piezo stage.

The 2D Raman maps (25 × 25 pixels) in **Figure 3.3d (left column)** clearly show the spatial intensity distribution between the top and bottom surface of micro-/nano-optoelectrodes for the electronic Raman scattering (ERS) peak (I_{ERS}) at 79 cm^{-1} and BZT Raman scattering peaks at 417 cm^{-1} (I_{417}) and 1073 cm^{-1} (I_{1073}) with a relative standard deviation (RSD) of ≈110 %. (Note: RSD = $\sigma/\mu \times 100$ %, where σ is the standard deviation, and μ is the mean.) Such broad RSD manifests the SERS measurement variations in plasmonic nanoantenna geometries and laser excitation focus conditions, making quantitative SERS analysis difficult. Our recent research has shown that plasmon-enhanced ERS signals from metal can serve as an internal standard for spatial and temporal SERS calibration[72]. As shown in **Figure 3.3d (right column)**, the ERS-calibrated 2D SERS maps for I_{417}/I_{ERS} and I_{1073}/I_{ERS} exhibit a much-reduced RSD from ≈100 % and ≈110 % to ≈12 % and ≈13 %, comparable to the I_{417}/I_{1073} RSD value of ≈14 % by self-calibration between two vibration modes of the BZT molecule. After the ERS calibration, the slight spatial uniformity in 2D SERS maps is likely due to Raman scattering cross-section variations from inhomogeneous molecule orientation arrangement in the surface-modified BZT monolayer. We envision that ERS calibration can significantly improve quantitative SERS biochemical analysis of molecule concentrations from the top and bottom surface of micro-/nano-optoelectrodes for future bio-sensing applications.

3.3.3. Numerical Analysis of Microscopic Mode Characteristics

To understand the measured far-field response in the context of microscopic near-field interactions from plasmon excitation, we use numerical finite-difference-time-domain (FDTD) simulations to calculate the far and near-field optical response with a model of the micro-/nano-optoelectrode based on the estimated dimensions from the SEM images shown in **Figure 3.1 and Figure 3.2.** SEM images clearly show nanoantenna size variation on the micropillar domes. Hence, to better understand the size-dependent optical response, we calculate the reflectance spectra for a select range of radii, matching estimates from SEM images including r = 62 nm, 66 nm, and 70 nm (**Figure 3.5a**).

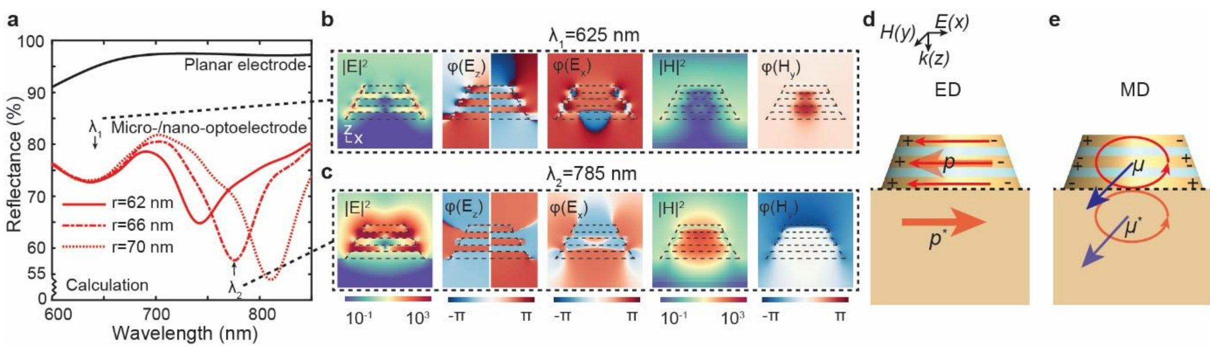

Figure 3.5 Microscopic multiresonant behaviors with loading effects of the metal ground plane. (a) FDTD calculated reflectance spectra of the micro-/nano-optoelectrodes with different nanoantenna diameters compared to the planar electrode. (b) FDTD calculated near-field distribution maps of normalized $|\boldsymbol{E}|^2$, $\varphi(E_z)$, $\varphi(E_x)$, $|\boldsymbol{H}|^2$, and $\varphi(H_y)$ in the *x-z* plane for resonant modes at l_1 = 625 nm and (c) l_2 = 785 nm. (d) Microscopic scheme of l_1 mode due to destructive interference of electric dipole (ED) mode in nanolaminate nanoantennas and its out-of-phase image ED in the ground mirror plane. (e) Microscopic scheme of l_2 mode due to constructive interference of magnetic dipole (MD) mode in nanolaminate nanoantennas and its in-phase image MD in the ground mirror plane.

FDTD calculated far-field plots reveal several distinct characteristics of micro-/nano-optoelectrode. First, consistent with the measurements in **Fig. 3.3a**, the planar electrode shows a high reflectance in a wavelength range of 600 nm to 850 nm due to a low penetration depth of optical fields into the metal (**Figure 3.5a**). Second, in agreement with measurements, FDTD calculated reflectance spectra of the micro-/nano-optoelectrode show a broadband absorption from 600 nm to 850 nm with two resonant modes at λ_1 and λ_2. Third, the micro-/nano-optoelectrode reflectance spectral reveals that the λ_1 mode remains fixed in spectral position (≈ 640 nm) and reflectance when increasing nanoantenna base radius from r = 62 nm to r = 70 nm, whereas the λ_2 mode redshifts from 730 nm to 810 nm with a correspondingly larger dip in reflectance. The measurements also reveal such double-resonant characteristics of micro-/nano-optoelectrode with two spectral dips at ≈ 690 nm and ≈ 760 nm (see **Figure 3.3a**). Differences between the measurement and simulation can be attributed to fabrication-related surface roughness, homogenous and inhomogeneous broadening effects, and plasmon damping from interfacial 1 nm thick Cr adhesion layer between Au and SiO_2.[73]

To investigate the microscopic nature of the modes supported in micro-/nano-optoelectrodes, we calculate the near-field distribution maps of normalized intensity ($|E|^2$ and $|H|^2$) and phase ($\varphi(E_z)$, $\varphi(E_x)$, $\varphi(H_y)$) for the two modes at $\lambda_1 \approx 640$ nm (**Figure 3.5b**) and $\lambda_2 \approx 785$ nm (**Figure 3.5c**) in micro-/nano-optoelectrodes with r = 66 nm. The 2D near-field plots reveal several distinct mode characteristics that differ from the same nanoantenna arrangement without the conductive micropillar (ground plane) (**Figure 3.6**).

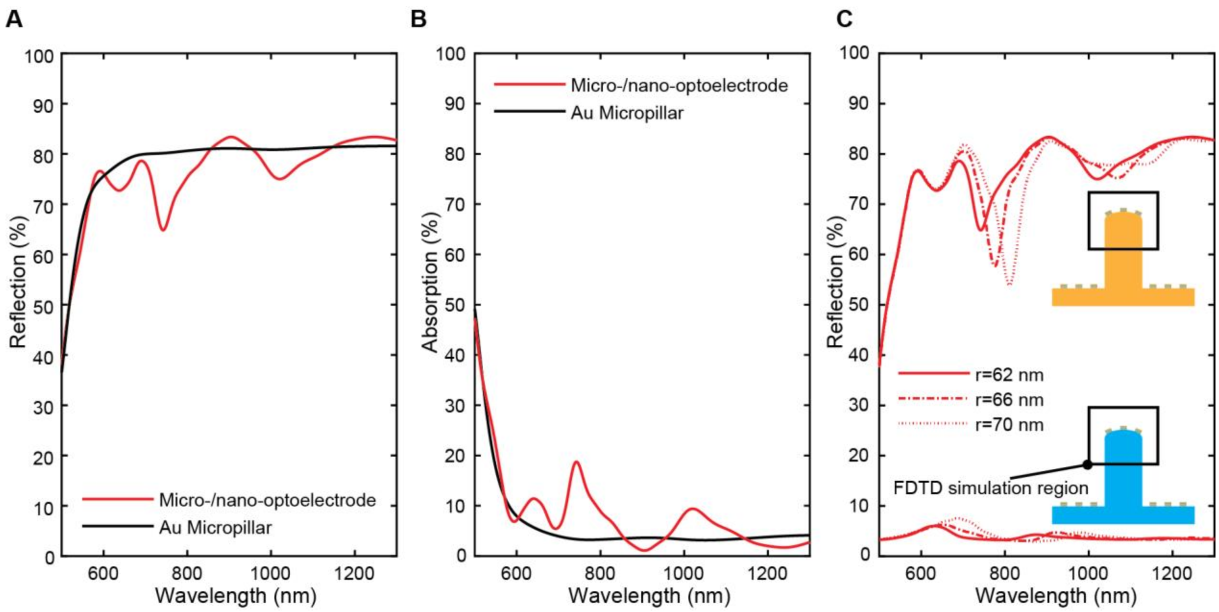

Figure 3.6 FDTD-calculated optical response. (a) Reflection and (b) absorption spectra for both micro-/nano-optoelectrode and Au micropillar. (c) Reflection spectra for dielectric and conductive micro-/nano-optoelectrode with nanoantennas of increasing diameter from 124 nm to 140 nm.

First, **Figure 3.5b** shows that the λ_1 mode exhibits (*i*) electric dipole (ED) characteristics with an in-phase $\varphi(E_x)$ distribution in three Au nanodisks except for an out-phase $\varphi(E_x)$ in the bottom nanodisk extended below the metal surface and (*ii*) weak magnetic response within and around the nanoantenna shown in the $|H|^2$ distribution map. As a comparison, the λ_1 mode in the nanoantenna with ground plane shows a substantial suppression of intensity (normalized $|E|^2$ $<10^2$), while the λ_1 mode in the nanoantenna without a ground plane (in the air) support enhanced intensity (normalized $|E|^2 > 10^3$) to penetrate into the dielectric gap nanocavities (**Figure 3.7**).

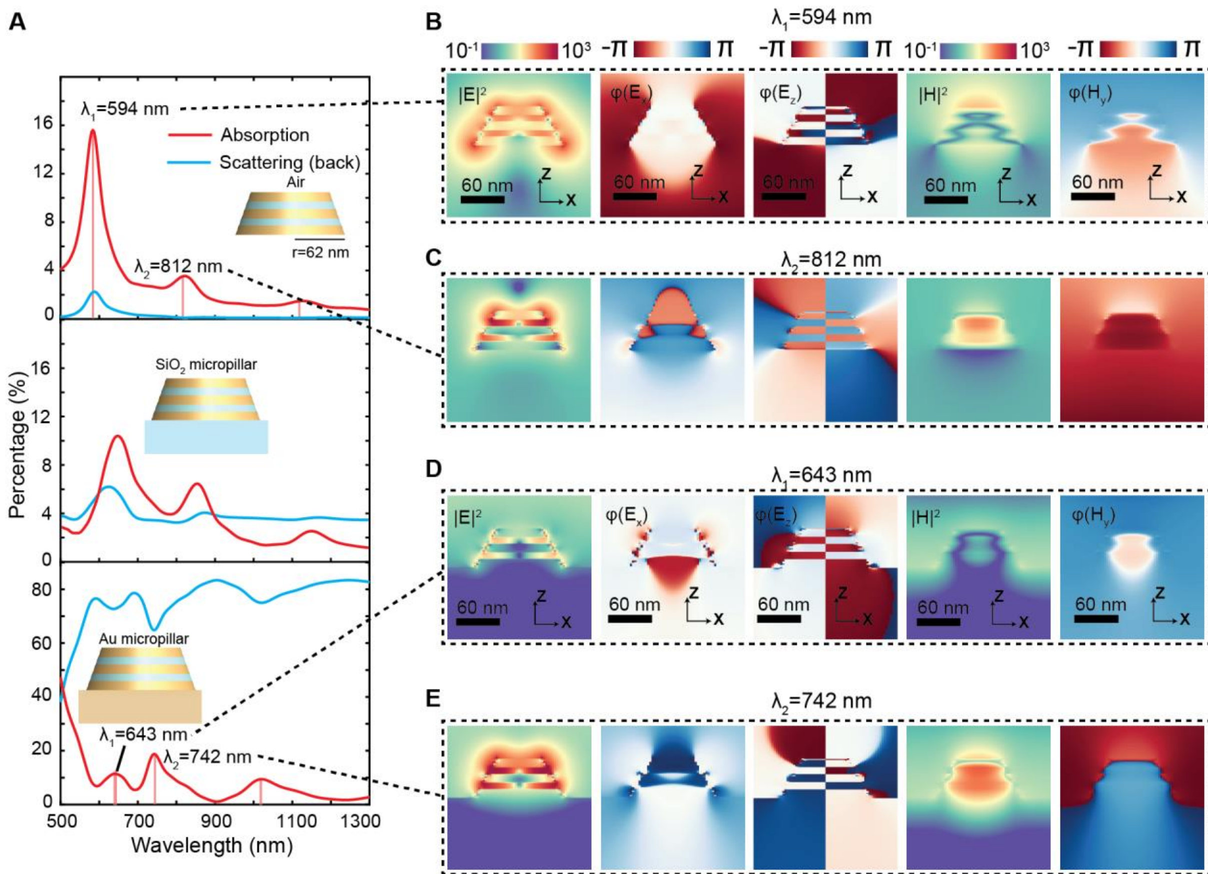

Figure 3.7 FDTD-calculated far- and near-field response of nanoantenna in air and on a SiO_2 and Au micropillar (ground plane). (a) Absorption and backscattering for nanoantenna in air and on a SiO_2 micropillar and Au ground plane. (b-e) FDTD calculated near-field distribution maps of $|E|^2$, $\varphi(E_z)$, $\varphi(E_x)$, $|H|^2$, and $\varphi(H_y)$ at the *x-z* plane for resonant modes at (b) l_1 = 594 nm and (c) l_2 = 812 nm for nanoantenna in air and (d) l_1 = 643 nm and (E) l_2 =742 nm on ground plane.

Next, the near-field plot of the mode at λ_2 = 785 nm reveals (*i*) magnetic dipole (MD) characteristics with high magnetic fields in both bottom and top nanocavities and in-phase $\varphi(H_y)$ in and below the nanoantenna, and (*ii*) electric quadrupole (EQ) characteristics where the top and middle Au nanodisks show an out-of-phase $\varphi(E_x)$ distribution compared to the bottom Au nanodisk (**Figure 3.5c**). Furthermore, spatially distributed magnetic fields that extend below the nanostructure are not observed for nanoantennas in the air (**Figure 3.7**), revealing the ground-plane loading effects from the conductive surfaces that provide an additional degree of mode engineering by mirror-mode coupling.[74-76] Lastly, we can see the large intensity region (normalized $|E|^2 > 10^3$) uniformly distributed within and around the top and bottom nanocavities, indicating that image-induced coupling affects the microscopic characteristics for the λ_2 mode, including an enhanced optical field intensity, spatial distribution, and magnetic response.[77]

Figure 3.5d illustrates the interaction of the ED mode in the nanolaminate nanoantenna with its image in the ground plane (highly conductive surface), where the electric dipole parallel to the surface couples with its out-of-phase mirror image electric dipole to generate a bonding

EQ mode with reduced optical cross-section and red-shifted resonant wavelength. **Figure 3.5e** illustrates the interaction of the MD mode in the nanolaminate nanoantenna with its image in the ground plane, where the magnetic dipole couples with its in-phase mirror image magnetic dipole to generate an antibonding MD mode with the increased optical cross-section and blue-shifted resonant wavelength.[78] Furthermore, FDTD calculations reveal that a nanolaminate nanoantenna on the ground plane can support a lower energy magnetic quadrupole (MQ) mode around 1000 nm with an increased optical cross-section than the case in air (without a ground plane) (**Figure 3.7**), manifesting that a magnetic quadrupole can constructively interact with its image in the mirror, altering the intrinsic radiation properties via an antenna loading effect analogous to its radio-frequency counterpart.[79]

3.3.4. Measured Electrode Properties

To understand the potential interfacial dynamics that can influence electrode electrochemical (EC) characteristics in biological solutions, we used 1× PBS with a nominal pH of ≈7.4 to mimic similar osmolarity and ion concentration typically found in isotonic physiological conditions. Using a custom EC-cell, we conducted electrochemical impedance spectroscopy (EIS) and cyclic voltammetry (CV) to probe the double-layer capacitance and diffusion characteristics at the electrode-electrolyte interface (**Figure 3.8**).

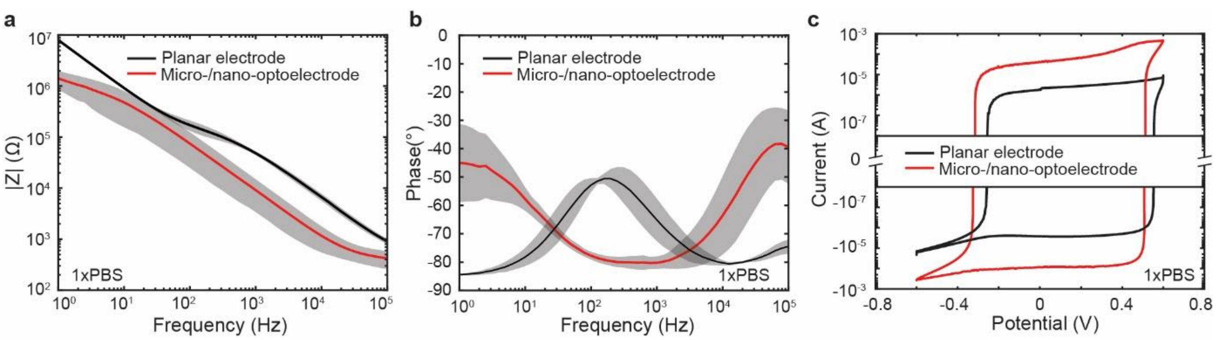

Figure 3.8 Electrode properties from electrochemical impedance spectroscopy (EIS) and cyclic voltammetry (CV) measurements. (a) Measured impedance magnitude |*Z*| spectra, (b) measured bode phase plot with the marked (shaded) experimental statistical uncertainties being one standard deviation, and (c) measured voltammogram in log scale for the micro-/nano-optoelectrodes and the planar electrode in 1× phosphate-buffered saline (1× PBS).

The average response of individual EIS spectra is measured from three randomly picked electrode units. Every electrode spectrum consists of ten frequency points per decade averaged from ten measures per frequency. As shown in **Figure 3.8a-b**, the solid line is the mean spectrum, and the shaded region represents the one standard deviation statistical uncertainty. The relative uncertainty in the impedance magnitude and phase is larger for micro-/nano-optoelectrode than for the planar electrode, indicating the sensitive dependence of the interfacial electrochemical behaviors on micro-/nano-structured surface topology. Geometrical variations of surface topology for different micro-/nano-optoelectrodes can be attributed to the partial misalignment between the nanoantenna array and electrode 2D spatial area, as shown in **Figure 3.2**. However, with an overall increase in surface area, micro-/nano-optoelectrodes exhibit an order-of-magnitude reduction in impedance magnitude (|*Z*|) compared to the planar electrode in a frequency range of 1 Hz to 100 kHz. Specifically, for the typical action potential frequency around 1 kHz, $|Z|$ reduces from 60 kΩ for the planar electrode to 5 kΩ for the micro-/nano-optoelectrode (**Figure 3.8a**), manifesting the inverse dependence of impedance on surface area ($Z \propto A^{-1}$) due to the hierarchical geometry.[80]

Next, the impedance phase plot reveals three distinct regions within the frequency spectrum from 1 Hz to 100 kHz where micro-/nano-optoelectrodes differ distinctly from the planar electrode (**Figure 3.8b-c**). In the low-frequency band between 1 Hz and 10 Hz, the micro-/nano-optoelectrode has a larger phase (–60°) than the planar electrode (–90°), indicating diffusion-limited ion transfer current and modified interfacial ionic double layer in hierarchical geometries.[81] In the intermediate-frequency band between 100 Hz and 1 kHz, the planar electrode shows an increased phase from –90° to –45°; in contrast, the micro-/nano-optoelectrode exhibits a reverse trend with a reduced phase from –60° to –85°, revealing a transition of the dominant current from the longer-range ion diffusion to the short-range charging-discharging in the electric double-layer capacitor (EDLC).[82] In the high-frequency band between 10 kHz and 100 kHz, the phase for the planar and micro-/nano-optoelectrode is –90° and –30°, respectively, revealing another reversal in characteristics where the planar electrode now behaves as an EDLC while the response of micro-/nano-optoelectrode is affected by ion transport limitation and non-uniform pathway for ion transport from the bulk electrolyte.[82, 83] **Figure 3.8c** shows the CV curves in a decadic logarithm scale to illustrate the magnitude differences in the current response between planar and micro-/nano-optoelectrodes (linear CV plot reproduced in **Figure 3.9**).

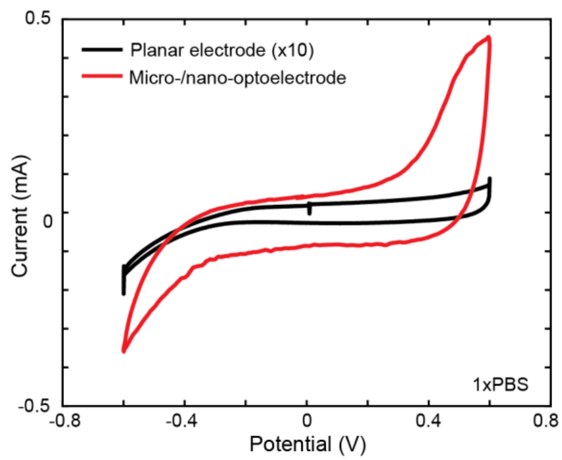

Figure 3.9. **Cyclic voltammogram with linear current scale for planar electrode and micro-/nano-optoelectrode.**

With a relatively slow scan rate of 50 mV/s, the CV measurements can approach a quasi-static electrochemical interface in the low-frequency limit. Under the applied working electrode potential from –0.6 V to 0.6 V, the planar electrode generates a current response between -10^{-5} A and 10^{-5} A, while the micro-/nano-optoelectrode produces a two-order of magnitude higher current response between -10^{-3} A and 10^{-3} A. Compared to the planar electrodes, the increased surface area of micro-/nano-optoelectrode contributes to a larger EDLC, as indicated by the larger area enclosed in the voltammogram trace.[84]

3.3.5. Nyquist Plot and Equivalent Circuit Modeling

To better understand the enhancement of electrochemical performances by introducing the micro-/nano-structures, we have performed an equivalent circuit model simulation to analyze and fit the measured Nyquist impedance plots (**Figure 3.10)**.

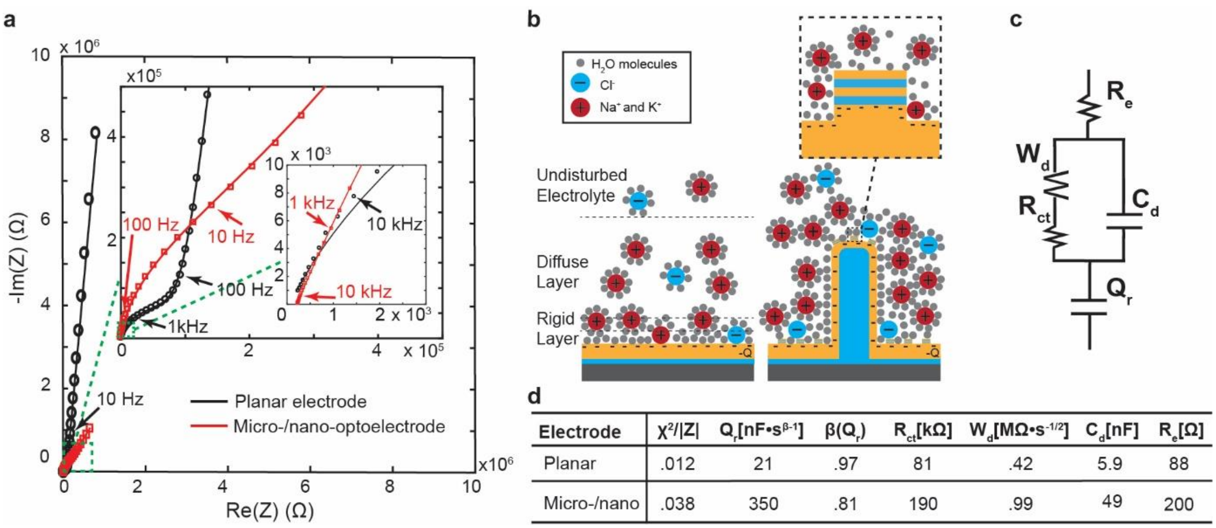

Electrode	$\chi^2/\lvert Z\rvert$	Q_r[nF•s$^{\beta-1}$]	$\beta(Q_r)$	R_{ct}[kΩ]	W_d[MΩ•s$^{-1/2}$]	C_d[nF]	R_e[Ω]
Planar	.012	21	.97	81	.42	5.9	88
Micro-/nano	.038	350	.81	190	.99	49	200

Figure 3.10 Nyquist plot and circuit modeling. (a) Measured Nyquist plots and fitted curves based on circuit modeling for the micro-/nano-optoelectrode and the planar electrode in 1× PBS. The inset shows the high-frequency components of the Nyquist plots. (b) Schematic illustration of electrode-electrolyte interface. (c) Equivalent circuit model. (d) The table of fitted results for components used in the equivalent circuit model.

By decomposing the real and imaginary parts of the measured impedance in a Nyquist plot, shown as black and red circles in **Figure 3.10a**, we can extrapolate the general resistive (real part) and capacitive reactance (negative of the imaginary part) characteristics of planar electrode and micro-/nano-optoelectrode impedance. First, in the low-frequency regime between 1 Hz to 10 Hz (1 Hz is the first data point furthest from the origin), the planar electrode shows a more significant slope with larger capacitance (≈ 8x). In contrast, micro-/nano-optoelectrodes show a smaller slope near unity, indicating that the 3D geometry of micro-/nano-optoelectrode affects the diffusion-related mass transport processes in the low-frequency limit and thus the equilibrium differential capacitance.[82] Also, we should note that the unity slope in micro-/nano-optoelectrode does not necessarily suggest an ideal semi-infinite planar electrode case since our EC cell has a finite volume with additional impedance from the connection and substrate components. On the contrary, the slope of the planar electrode in the low-frequency limit turns out to be much larger than one, which is due to the reasons above. Second, in the intermediate frequency (100 Hz to 1 kHz), while the planar electrode shows a rapid slope decrease with frequency, micro-/nano-optoelectrodes show a gradual increase in slope with the frequency, indicating that non-overlapped diffusion layers of adjacent micropillars can contribute to increased capacitive attributes.[81, 85] Third, in the high-frequency regime (10 kHz to 100 kHz), while the slope of the planar electrode increases to a vertical trend, the slope of the micro-/nano-optoelectrode increases then plateaus slightly, manifesting changes to a compact EDLC at the interface, likely due to ion mobility limits at high-frequencies.

We select the electrical circuit modeling elements to fit the measured Nyquist plots by considering several interfacial processes for microscopic anions, cations, and water molecules at the electrode-electrolyte interface during electrochemical equilibrium with a zero direct current. Notably, the general electrode-electrolyte interface consists of three spatial regions, including rigid layer, diffuse layer, and undisturbed electrolyte, which can be modeled with corresponding lumped circuit elements in **Figure 3.10c.** First, a layer defined as the inner Helmholtz plane is established from the hydration of the metal surface with polar water molecules due to the electrostatic attraction to excess surface charges. There are rigidly held counterions on the water layer that resist thermal motion, which define the outer Helmholtz plane represented as red circles for sodium and potassium cations in PBS in **Figure 3.10b**. The rigidly held counterions separated by water molecules from the metal surface charges comprise the first electrochemical structure, which is known as the rigid layer (or Helmholtz double layer). A constant phase element (CPE) can model the rigid layer to account for variations in the orientation polarization of water molecules, resulting in an electrochemical equivalent of a leaky capacitor with an imperfect dielectric layer.[86] The impedance of the CPE is expressed as, $Z_{CPE}(f) = \frac{1}{Q(j2\pi f)^{\beta}}$, where Q is the CPE (nonideal capacitance) with units $F \cdot s^{\beta-1}\ where\ s = j2\pi f$, f is the frequency in Hertz, $j = \sqrt{-1}$, and $\beta \in [0,1]$ is an ideality factor (note: β = 1 yields the impedance of an ideal capacitor).[87] Intercalation of specifically adsorbed anions (chloride ions, blue circles) within the inner Helmholtz plane is also possible due to short-range chemical adhesive forces, *e.g.*, Van der Waals interactions, leading to direct bonding to the metal surface where local chemical bonding forces are not saturated because of the local specific crystallographic structure or due to local defects of the crystal lattice.[86] Beyond the rigid layer, other counterions (space charges) are mobile, collectively constructing a cloud of space charge defined as the diffuse layer (or Gouy-Chapman double layer) with a thickness defined as the Debye length. Conventionally, within the diffuse region, we can use a semi-infinite linear diffusion Warburg element (W_d) to account for diffusion from spatial concentration gradients of the different dissolved ions in the electrolyte.[86] The Warburg element (W_d) can build on the constant phase element, $Z_{CPE}(f) = \frac{1}{Q(j2\pi f)^{\beta}}$, by setting β=0.5. Current in the diffuse regions can travel through two pathways. The first pathway mediates the faradic current through the Warburg element (W_d) and charge-transfer resistance (R_{ct}). The second pathway mediates the non-faradic current associated with the charging and discharging of the Gouy-Chapman double-layer capacitance (C_d). Since the EIS measurements are performed in PBS, an inert electrolyte without redox-active species, the direct charge transfer between the electrode-electrolyte interface is relatively small, resulting in a dominant non-faradic current pathway in the current model.[82] Therefore, the charge-transfer resistance in this context is likely due to the adsorption and desorption processes of monolayer Cl- ions on the Au surface, which can contribute to a small Faradaic current.[88] The third and last region is the undisturbed electrolyte layer, where cation and anion concentrations are equal and can be modeled with electrolyte resistance (R_e), which may also include parasitic contact and equipment resistance contributions in the circuit.

The circuit model parameters used to fit the measured Nyquist plot in **Figure 3.10a** were obtained by the Levenberg-Marquardt minimization algorithm, which was based on yielding the lowest $\chi^2/|Z|$ value, resulting in 0.012 Ω and 0.038 Ω, respectively, for the planar and micro-/nano-optoelectrode. The weighted $\chi^2/|Z|$ is an indicator of goodness of fit and estimates the distance between the measured data and the simulated data. The expression is given by, $\chi^2/|Z| = \sum_{i=1}^{N} |Z_i(f_i) - Z(f_i)|^2/|Z(f_i)|$ where Z_i is the measured impedance and $Z(f_i)$ is the value of the impedance calculated at a frequency f_i for a defined set of circuit parameter values and the number of points N of the iterated minimization algorithm. The minimization process yields the corresponding circuit parameters, shown in **Figure 3.10d**, with a deviation parameter. The deviation (dev) parameter can be assimilated to a standard deviation, and it conveys an estimate of the relevancy of the parameter, i.e., if dev is relatively large, then its variation in value will not affect the quality of the fit, rendering it uncritical in the minimization process, and indicating that the circuit needs simplification or the physical basis for the circuit model is invalid. Therefore, the dev parameter can assess the uncertainty in the circuit model's ability to recapitulate the underlying frequency-dependent impedance dynamics from the microscopic electrode-electrolyte interfacial processes. As was previously the case for **Figure 3.10a**, there is an uncertainty in the surface area and topology of different 3D electrodes, resulting in a unique set of circuit parameters for each 3D electrode, but the circuit model generally remains applicable to all. We extract the component values from the equivalent circuit model fit to reveal several unique characteristics. First, we find that the R_{ct} value for micro-/nano-optoelectrodes ($R_{ct} \approx 190$ kΩ, dev ≈ 17 Ω) is higher than planar electrodes ($R_{ct} \approx 81$ kΩ, dev ≈ 2.7 Ω) despite their larger surface area, which is likely due to the slight polymer residue on micro-/nano-optoelectrodes from extra photoresist spin-coating involved nanofabrication processes. Second, the Warburg parameter for micro-/nano-optoelectrodes ($W_d \approx 1$ MΩ· $s^{-0.5}$, dev ≈ 75 Ω· $s^{-0.5}$) has a larger value than planar electrodes ($W_d \approx 0.4$ MΩ· $s^{-0.5}$, dev ≈ 60 Ω· $s^{-0.5}$), suggesting that their larger diffusive layer thickness contributes to a decrease in capacitance offset by an increase in surface area. Third, the double-layer capacitance for micro-/nano-optoelectrodes (C_d ≈ 49 nF, dev ≈ 6 × 10^{-3} nF) is one order larger than planar electrodes (C_d ≈ 6 nF, dev ≈ 2 × 10^{-3} nF), revealing that the total surface area plays a more significant role while the larger diffusive layer thickness is less significant to affect the total double-layer capacitance. Next, the thickness of the rigid layer is constrained by the effective radius of solvated counterions (≈ 0.1 nm), so the one-order in magnitude increase in Q_r from ≈ 21 nF· $s^{\beta-1}$ (dev ≈ 4 × 10^{-6} nF· $s^{\beta-1}$) to ≈ 350 nF· $s^{\beta-1}$(dev ≈ 1 × 10^{-2} nF· $s^{\beta-1}$) is mainly due to increased surface area and effective surface roughness between planar electrodes and micro-/nano-optoelectrodes. Compared to the planar electrode with β = 0.97, resembling the ideal capacitor, the micro-/nano-optoelectrode with β= 0.81 shows a nonideal capacitance behavior due to its micro-/nanostructured surface inhomogeneities within the inner Helmholtz plane, where the distribution and dipole moment orientation for water molecules, and surface adsorbed anions/cations can vary significantly at different locations.[89] Lastly, R_e for micro-/nano-optoelectrode (R_e ≈ 200 Ω, dev ≈ 0.3 Ω) is larger than the planar electrode (R_e ≈ 90 Ω, dev ≈ 0.4 Ω), which may be associated with the different distances between their working and counter electrodes in the EC-cell.

3.4 Conclusion

A top-down modular fabrication procedure was developed to pattern nanolaminate nanoantennas on micropillar electrode arrays, enabling tunable hybrid optical-electrical functionality in a single device. Optical and electrical functionality dependent on structural geometry can be tuned by controlling design and processing parameters such as micropillar diameter and PVD deposition thickness. Experimental and calculated far-field optical spectra reveal multiple resonant plasmonic modes. Our calculated near-field 2D maps show that nanolaminate nanoantennas on the ground plane can enjoy enhanced magnetic field intensities within dielectric nanocavities due to the interactions with its image mode as a result of the ground-plane-like loading effect.[90] Electrochemical impedance spectroscopy and cyclic voltammetry provided insights into area-dependent microscopic electrochemical dynamics at the electrode-electrolyte interface with unique characteristics that warrant further investigation. We envision that micro-/nano-optoelectrode arrays can serve as a multifunctional platform for monitoring and modulating cellular systems. Specifically, the proposed system-level modular design method can overcome challenges in achieving tight cell-device coupling and optimized hybrid device properties for achieving multimodal bioelectrical recording and SERS biochemical analyses with minimal perturbation to intrinsic cellular functions. Lastly, the proposed design approach can be generalized to incorporate 3D printing of micro-/nano-scale templates using stereolithography or 2-photon lithography to further expand the design space of complex 2D and 3D patterns for hierarchically structured micro-/nano-optoelectrodes. Such a focus on modularized design and fabrication will facilitate the systematic development of multimodal bio-machine interfacing systems for biological and medical applications using chip-based or flexible mesh-based substrates.

3.5 Methods

3.5.1 Fabrication and Transfer of AuNHA on Hierarchical Surfaces

To create AuNHA deposition masks, we used our established protocol adapted from the phase-shifting photolithography, etching, electron-beam deposition and lift-off (PEEL) technique.[38] Briefly, we used a free-standing film of AuNHA as a physical deposition mask to create periodic arrays of discrete multilayered nanoantennas. To fabricate AuNHA, we first used a poly(dimethylsiloxane) (PDMS) photomask replicated from a silicon master patterned with nanopillar arrays to expose a positive-tone photoresist (PR) on a silicon wafer in contact mode. After exposure and development of PR nanopillar arrays, we deposited a thin Cr layer (nominally 10 nm) using physical vapor deposition (PVD) by electron-beam (e-beam) evaporation, followed by sonication with acetone to lift off the nanopillar arrays and create Cr nanohole arrays on the silicon wafer. Using reactive ion etching with O_2 and CF_4 mixtures (1:5), we etched an undercut in the silicon wafer under the Cr nanohole arrays, followed by the e-beam PVD of approximately 160 nm thick Au layer on top of the Cr. We then lifted off AuNHA using Cr etchant and handled the thin film with a plasma-treated glass slide, scooping it from the Cr etchant dish and transferring it to a water-filled dish. We transferred the AuNHA onto the micropillar electrode array from the water dish by suspending and transporting the AuNHA in a water droplet on the glass slide. After transferring AuNHA by tilting the glass slide over the center of the MEA, we allowed the water droplet underneath the AuNHA to evaporate steadily at room temperature. Note that the rapid evaporation by applied heat can result in the AuNHA film wrapping/compressing onto the pillar.

3.5.2 Fabrication of Micro-/nano-optoelectrode Arrays

The fabrication of micro-/nano-optoelectrode begins by precleaning a three-inch diameter Si wafer with oxygen plasma (50 W, 1 min, 50 cm^3/min of O_2) and followed by spin-coating with positive-tone photoresist (PR) at 3000 revolutions per min for 30 s. The resist is then prebaked on a hotplate set for 2 min at 95 °C, and the mask design #1, containing micropillar arrays, is exposed onto SU8 using a maskless aligner (direct-write photolithography, DWPL). We leveraged the automated features of the DWPL tool to quickly generate a focus-exposure matrix, allowing us to determine the optimal exposure dose around 100 mJ/cm^2 with the 375 nm laser and optimal defocus value around 0. After PR exposure, the exposed PR on the silicon wafer is baked using a hot plate for 3 min at 95 °C, and the pattern is developed by immersing the wafer in a dish containing SU8 developer for approximately 2 min to 3 min. Next, the wafer is rinsed with isopropyl alcohol and blow-dried with N_2 flow. Lastly, the target SU8 micropillar structures on the silicon wafer are hard baked at 180 ºC for 45 mins. Following a similar procedure, we prepared a bilayer resist stack by first spin-coating a lift-off resist at 3000 revolutions per min for 45 s, followed by baking on a hotplate set at 180 °C for 5 mins; the second layer consisting of positive photoresist is spin-coated at 4000 revolutions per min and baked at 115 °C for 1 min. We exposed our mask design #2, which consisted of the microelectrodes, contact pads, and lines. Similar to before, a focus-exposure matrix was used to find the optimal exposure and focus with 405 nm wavelength laser conditions around 150 mJ/cm^2 and 0, respectively. Alignment markers were patterned to ensure proper overlap between each square microelectrode and 4 x 4 micropillar array. After PR exposure, the wafer is immersed in tetramethylammonium hydroxide (TMAH) for approximately 1 min and 40 s to create an undercut in the lift-off layer and transferred to a dish containing deionized (DI) water for 30 s to stop the development process. We rinsed any excess exposed PR with DI water, gently streamed from a wash bottle. Any excess resist beyond development can be "descummed" using plasma treatment, but we found the procedure worked successfully without descumming before deposition. We used the direct current and radio-frequency sputtering guns in a commercial sputtering PVD system to deposit 10 nm of SiO_2, 30 nm of Cr, and 100 nm of Au while the substrate rotated. Sputter PVD is followed by the spin-coating of a positive PR which was then soft-baked and exposed to define a clear window for only the 64 square microelectrode regions with the rest of the wafer being masked. The prefabricated AuNHA was then transferred onto the wafer, and e-beam PVD was conducted without substrate rotation to deposit alternating layers of 12 nm thick Au and 9 nm thick SiO_2 layers with 1 nm thick Ti interfacial adhesion layer between each metal-insulator interface. The deposition was performed at a high vacuum < 1.33×10^{-4} Pa. After e-beam PVD, the wafer was submerged in a double PR stripper bath for 2 h, with the development processes accelerated by periodic agitation from shaking the bath dish. After completing the lift-off process, a final passivation layer composed of SU8 can be spin-coated, prebaked, exposed, post-exposure baked, developed, and hard baked similarly as the micropillar fabrication procedure. Additionally, mesh electronics can be derived from this fabrication procedure by including a Ni sacrificial layer and a bottom passivation layer before creating the SU8 micropillars.

3.5.3 Micro-reflectance Measurement

Reflectance measurements were done using a halogen lamp coupled to an input optical fiber connected to a confocal microscope through an adapter with a collimation lens. After passing a 50/50 beam splitter, the unpolarized light was focused at normal incidence and captured using a 50x objective with a numerical aperture (NA) of 0.75. After passing the 50/50 beam splitter, the reflected light was collected/coupled with an output optical fiber, serving as a pinhole for spatial filtering. The output optical fiber is routed to a spectrometer. An integration time of 0.1 s was used, and an accumulation of 10 spectra was acquired for 7 single micro-/nanoelectrodes, which were then averaged to obtain the spectra shown in **Figure 3.3a**. Normalization of the incident white light spectral profile and intensity was performed with a silver mirror.

3.5.4 FDTD Simulation

As a first-order approximation, a finite 3x3 array of nanoantennas on a planar-top gold micropillar with a diameter of 2.5 µm substrate was used to simulate the response from the top of the micropillar. Optical constants of Au were taken from Johnson and Christy[91] in the spectrum range from 500 nm to 900 nm, and n = 1.5 was used for SiO_2. A fine mesh with the geometry 200 nm x 200 nm x 200 nm and mesh resolution of x = y = 3 nm and z = 1 nm was used for all nanolaminate nanoantennas. A Gaussian beam was used as the excitation source with a waist diameter of 2.6 µm, and the boundary conditions were satisfied with a phase match layer on all quadrants.

3.5.5 BZT Raman Measurements and SERS Enhancement Factor

Samples were incubated in an ethanol-based 1 mmol/L BZT solution for 24 h, followed by ethanol rinsing to form a self-assembled monolayer on the electrode surface. SERS measurements were done under laser excitation at a wavelength of 785 nm and power of 1 mW via a 50×objective (NA = 0.75) with a commercial confocal microscope in the backscattering configuration. 2D Raman maps were acquired at a 1 s integration time per pixel over a 35 µm × 35 µm area using a piezo stage to scan the samples and a CCD camera in a commercial spectrometer to measure the Stokes Raman scattering. A long-pass filter was used to block elastically scattered light at the wavelength corresponding to the laser line (Rayleigh scattering), and the Stokes scattering passed through a multimode fiber (100 µm core diameter) with the cleaved fiber core acting as the confocal pinhole. The SERS EFs were calculated based on our past work using the following relation, $EF = (I_{SERS}/I_{Raman}) \times (N_{Raman}/N_{SERS})$. I_{SERS}, I_{Raman}, N_{SERS}, and N_{Raman} are the SERS BZT intensity, neat BZT Raman intensity, and the number of BZT molecules contributing to SERS and neat Raman intensities, respectively. I_{SERS} (1073 cm^{-1}), which corresponds to the C-C-C ring in-plane breathing mode, was used for the EF calculations. N_{SERS} was calculated by $N_{SERS} = SA \times \rho_{SERS}$, where SA is the metal surface area contributing to the enhancement of Raman signal and ρ_{SERS} is the packing density of BZT on Au surface; The packing density of BZT molecules is $6.8 \times 10^{14}/cm^2$. N_{Raman} was calculated by $N_{Raman} = A \times d_{eff} \times \rho_{BZT}$, where A is the focused illumination area, d_{eff} is an effective depth; The number density of neat BZT, ρ_{BZT}, is $5.9 \times 10^{21}/cm^3$.

3.5.5 Electrochemical Measurement

Potentiostatic electrochemical impedance spectroscopy (EIS) was conducted with the working electrode voltage (E_{we}) set to zero vs. open circuit and a sinus amplitude of 10 mV. The equivalent circuit model assumes a current-less situation (I_{dc}=0) with no applied direct current or voltage. An Ag/AgCl saturated in KCl was used as the reference electrode, and a platinum coil was used as the counter electrode in a custom electrochemical cell (EC-cell) mounted to the sample using adhesive stripes. Phosphate buffer saline (PBS) was used as the electrolyte solution, composed of NaCl: 0.137 mol/L, KCl: 0.0027 mol/L, Na_2HPO_4: 0.01 mol/L, KH_2PO_4: 0.0018 mol/L for standard 1x PBS from commercial suppliers. Approximately 2 mL of 1x PBS was dropped into EC-cell, and measurements were done at room temperature. A potentiostat was used to perform EIS and cyclic voltammetry (CV), ranging from –0.5 V to 0.5 V in 100 mV/s increments. CV measurements were cycled several times until the EC system reached a steady state with the same CV profile shown in **Figure 3.8**.

References

1. Mejia, E.; Qian, Y.; Safiabadi Tali, S. A.; Song, J.; Zhou, W., Spectral tuning of double resonant nanolaminate plasmonic nanoantennas with a fixed size. *Applied Physics Letters* **2021,** *118* (24), 241108.
2. Ding, S.-Y.; Yi, J.; Li, J.-F.; Ren, B.; Wu, D.-Y.; Panneerselvam, R.; Tian, Z.-Q., Nanostructure-based plasmon-enhanced Raman spectroscopy for surface analysis of materials. *Nature Reviews Materials* **2016,** *1* (6), 16021.
3. Anker, J. N.; Hall, W. P.; Lyandres, O.; Shah, N. C.; Zhao, J.; Van Duyne, R. P., Biosensing with plasmonic nanosensors. *Nature Materials* **2008,** *7* (6), 442-453.
4. Pelton, M., Modified spontaneous emission in nanophotonic structures. *Nature Photonics* **2015,** *9* (7), 427-435.
5. Kauranen, M.; Zayats, A. V., Nonlinear plasmonics. *Nature Photonics* **2012,** *6* (11), 737-748.
6. Huang, X.; Jain, P. K.; El-Sayed, I. H.; El-Sayed, M. A., Plasmonic photothermal therapy (PPTT) using gold nanoparticles. *Lasers in medical science* **2008,** *23* (3), 217-28.
7. Bazard, P.; Frisina, R. D.; Walton, J. P.; Bhethanabotla, V. R., Nanoparticle-based Plasmonic Transduction for Modulation of Electrically Excitable Cells. *Sci Rep-Uk* **2017,** *7* (1), 7803.
8. Bonacina, L.; Brevet, P.-F.; Finazzi, M.; Celebrano, M., Harmonic generation at the nanoscale. *Journal of Applied Physics* **2020,** *127* (23), 230901.
9. Brongersma, M. L.; Halas, N. J.; Nordlander, P., Plasmon-induced hot carrier science and technology. *Nat Nanotechnol* **2015,** *10* (1), 25-34.
10. Baffou, G.; Quidant, R.; de Abajo, F. J. G., Nanoscale Control of Optical Heating in Complex Plasmonic Systems. *Acs Nano* **2010,** *4* (2), 709-716.
11. Safiabadi Tali, S. A.; Zhou, W., Multiresonant plasmonics with spatial mode overlap: overview and outlook. *Nanophotonics* **2019,** *8* (7), 1199-1225.
12. Payne, E. K.; Shuford, K. L.; Park, S.; Schatz, G. C.; Mirkin, C. A., Multipole Plasmon Resonances in Gold Nanorods. *The Journal of Physical Chemistry B* **2006,** *110* (5), 2150-2154.
13. You, E.-A.; Zhou, W.; Suh, J. Y.; Huntington, M. D.; Odom, T. W., Polarization-Dependent Multipolar Plasmon Resonances in Anisotropic Multiscale Au Particles. *Acs Nano* **2012,** *6* (2), 1786-1794.
14. Harutyunyan, H.; Volpe, G.; Quidant, R.; Novotny, L., Enhancing the Nonlinear Optical Response Using Multifrequency Gold-Nanowire Antennas. *Physical Review Letters* **2012,** *108* (21), 217403.
15. Thyagarajan, K.; Rivier, S.; Lovera, A.; Martin, O. J. F., Enhanced second-harmonic generation from double resonant plasmonic antennae. *Opt. Express* **2012,** *20* (12), 12860-12865.
16. Thyagarajan, K.; Butet, J.; Martin, O. J. F., Augmenting Second Harmonic Generation Using Fano Resonances in Plasmonic Systems. *Nano Letters* **2013,** *13* (4), 1847-1851.
17. Zhang, Y.; Wen, F.; Zhen, Y.-R.; Nordlander, P.; Halas, N. J., Coherent Fano resonances in a plasmonic nanocluster enhance optical four-wave mixing. *Proceedings of the National Academy of Sciences* **2013,** *110* (23), 9215.
18. Wang, H.; Brandl, D. W.; Le, F.; Nordlander, P.; Halas, N. J., Nanorice: A Hybrid Plasmonic Nanostructure. *Nano Letters* **2006,** *6* (4), 827-832.
19. Bardhan, R.; Mukherjee, S.; Mirin, N. A.; Levit, S. D.; Nordlander, P.; Halas, N. J., Nanosphere-in-a-Nanoshell: A Simple Nanomatryushka. *The Journal of Physical Chemistry C* **2010,** *114* (16), 7378-7383.

20. Mukherjee, S.; Sobhani, H.; Lassiter, J. B.; Bardhan, R.; Nordlander, P.; Halas, N. J., Fanoshells: Nanoparticles with Built-in Fano Resonances. *Nano Letters* **2010,** *10* (7), 2694-2701.
21. Hong, S.; Acapulco, J. A. I.; Jang, H. Y.; Park, S., Au Nanodisk-Core Multishell Nanoparticles: Synthetic Method for Controlling Number of Shells and Intershell Distance. *Chemistry of Materials* **2014,** *26* (12), 3618-3623.
22. Ozbay, E., Plasmonics: Merging Photonics and Electronics at Nanoscale Dimensions. *Science* **2006,** *311* (5758), 189.
23. Dipalo, M.; Messina, G. C.; Amin, H.; La Rocca, R.; Shalabaeva, V.; Simi, A.; Maccione, A.; Zilio, P.; Berdondini, L.; De Angelis, F., 3D plasmonic nanoantennas integrated with MEA biosensors. *Nanoscale* **2015,** *7* (8), 3703-3711.
24. La Rocca, R.; Messina, G. C.; Dipalo, M.; Shalabaeva, V.; De Angelis, F., Out-of-Plane Plasmonic Antennas for Raman Analysis in Living Cells. *Small* **2015,** *11* (36), 4632-4637.
25. Nel, A. E.; Mädler, L.; Velegol, D.; Xia, T.; Hoek, E. M. V.; Somasundaran, P.; Klaessig, F.; Castranova, V.; Thompson, M., Understanding biophysicochemical interactions at the nano–bio interface. *Nature Materials* **2009,** *8*, 543.
26. Poddubny, A.; Iorsh, I.; Belov, P.; Kivshar, Y., Hyperbolic metamaterials. *Nature Photonics* **2013,** *7* (12), 948-957.
27. Song, J.; Zhou, W., Multiresonant Composite Optical Nanoantennas by Out-of-plane Plasmonic Engineering. *Nano Letters* **2018,** *18* (7), 4409-4416.
28. Qian, Y.; Safiabadi Tail, S. A.; Mejia, E.; Zhou, W., Fixed-size double-resonant nanolaminate plasmonic nanoantennas with wide spectral tunability and high optical cross-sections. *Optik* **2021,** *230*, 166332.
29. Nam, W.; Song, J.; Safiabadi Tali, S. A.; Lezec, H. J.; Agrawal, A.; Zhou, W., Au/SiO2-Nanolaminated Plasmonic Nanoantennas as Refractive-Index-Insensitive and Transparent Surface-Enhanced Raman Spectroscopy Substrates. *ACS Applied Nano Materials* **2021,** *4* (3), 3175-3184.
30. Dmitriev, A.; Pakizeh, T.; Käll, M.; Sutherland, D. S., Gold–Silica–Gold Nanosandwiches: Tunable Bimodal Plasmonic Resonators. *Small* **2007,** *3* (2), 294-299.
31. Frederiksen, M.; Bochenkov, V. E.; Ogaki, R.; Sutherland, D. S., Onset of Bonding Plasmon Hybridization Preceded by Gap Modes in Dielectric Splitting of Metal Disks. *Nano Letters* **2013,** *13* (12), 6033-6039.
32. Kuttge, M.; García de Abajo, F. J.; Polman, A., Ultrasmall Mode Volume Plasmonic Nanodisk Resonators. *Nano Letters* **2010,** *10* (5), 1537-1541.
33. Maccaferri, N.; Zhao, Y.; Isoniemi, T.; Iarossi, M.; Parracino, A.; Strangi, G.; De Angelis, F., Hyperbolic Meta-Antennas Enable Full Control of Scattering and Absorption of Light. *Nano Letters* **2019,** *19* (3), 1851-1859.
34. Domina, K. L.; Khardikov, V. V.; Goryashko, V.; Nikitin, A. Y., Bonding and Antibonding Modes in Metal–Dielectric–Metal Plasmonic Antennas for Dual-Band Applications. *Advanced Optical Materials* **2020,** *8* (5), 1900942.
35. Schaffernak, G.; Krug, M. K.; Belitsch, M.; Gašparić, M.; Ditlbacher, H.; Hohenester, U.; Krenn, J. R.; Hohenau, A., Plasmonic Dispersion Relations and Intensity Enhancement of Metal–Insulator–Metal Nanodisks. *ACS Photonics* **2018,** *5* (12), 4823-4827.
36. Verre, R.; Yang, Z. J.; Shegai, T.; Käll, M., Optical Magnetism and Plasmonic Fano Resonances in Metal–Insulator–Metal Oligomers. *Nano Letters* **2015,** *15* (3), 1952-1958.

37. Ekinci, Y.; Christ, A.; Agio, M.; Martin, O. J. F.; Solak, H. H.; Löffler, J. F., Electric and magnetic resonances in arrays of coupled gold nanoparticle in-tandem pairs. *Opt. Express* **2008,** *16* (17), 13287-13295.
38. Henzie, J.; Lee, M. H.; Odom, T. W., Multiscale patterning of plasmonic metamaterials. *Nat Nanotechnol* **2007,** *2* (9), 549-554.
39. Mooradian, A., Photoluminescence of Metals. *Physical Review Letters* **1969,** *22* (5), 185-187.
40. Jiang, L.; Yin, T.; Dong, Z.; Liao, M.; Tan, S. J.; Goh, X. M.; Allioux, D.; Hu, H.; Li, X.; Yang, J. K., Accurate modeling of dark-field scattering spectra of plasmonic nanostructures. *Acs Nano* **2015,** *9* (10), 10039-10046.
41. Derkachova, A.; Kolwas, K.; Demchenko, I., Dielectric Function for Gold in Plasmonics Applications: Size Dependence of Plasmon Resonance Frequencies and Damping Rates for Nanospheres. *Plasmonics* **2016,** *11* (3), 941-951.
42. Alaee, R.; Albooyeh, M.; Yazdi, M.; Komjani, N.; Simovski, C.; Lederer, F.; Rockstuhl, C., Magnetoelectric coupling in nonidentical plasmonic nanoparticles: Theory and applications. *Physical Review B* **2015,** *91* (11), 115119.
43. Deng, S.; Li, R.; Park, J.-E.; Guan, J.; Choo, P.; Hu, J.; Smeets, P. J. M.; Odom, T. W., Ultranarrow plasmon resonances from annealed nanoparticle lattices. *Proceedings of the National Academy of Sciences* **2020,** *117* (38), 23380-23384.
44. Britton, W. A.; Chen, Y.; Dal Negro, L., Double-plasmon broadband response of engineered titanium silicon oxynitride. *Opt. Mater. Express* **2019,** *9* (2), 878-891.
45. Bin-Alam, M. S.; Reshef, O.; Mamchur, Y.; Alam, M. Z.; Carlow, G.; Upham, J.; Sullivan, B. T.; Ménard, J.-M.; Huttunen, M. J.; Boyd, R. W.; Dolgaleva, K., Ultra-high-Q resonances in plasmonic metasurfaces. *Nat Commun* **2021,** *12* (1), 974.
46. Gómez, D. E.; Teo, Z. Q.; Altissimo, M.; Davis, T. J.; Earl, S.; Roberts, A., The Dark Side of Plasmonics. *Nano Letters* **2013,** *13* (8), 3722-3728.
47. Hu, H.; Duan, H.; Yang, J. K. W.; Shen, Z. X., Plasmon-Modulated Photoluminescence of Individual Gold Nanostructures. *Acs Nano* **2012,** *6* (11), 10147-10155.
48. Mejia, E.; Song, J.; Zhao, Y.; Qian, Y.; Xiao, C.; Lezec, H. J.; Agrawal, A.; Zhou, W., Scalable two-tier protruding micro-/nano-optoelectrode arrays with hybrid optical-electrical modalities by hierarchical modular design. *Nanoscale* **2022,** *14* (41), 15373-15383.
49. Dixon, T. A.; Williams, T. C.; Pretorius, I. S., Sensing the future of bio-informational engineering. *Nature Communications* **2021,** *12* (1), 388.
50. Nuriya, M.; Fukushima, S.; Momotake, A.; Shinotsuka, T.; Yasui, M.; Arai, T., Multimodal two-photon imaging using a second harmonic generation-specific dye. *Nature Communications* **2016,** *7* (1), 11557.
51. Duan, X.; Gao, R.; Xie, P.; Cohen-Karni, T.; Qing, Q.; Choe, H. S.; Tian, B.; Jiang, X.; Lieber, C. M., Intracellular recordings of action potentials by an extracellular nanoscale field-effect transistor. *Nat Nanotechnol* **2012,** *7* (3), 174-179.
52. Xie, C.; Lin, Z.; Hanson, L.; Cui, Y.; Cui, B., Intracellular recording of action potentials by nanopillar electroporation. *Nat Nanotechnol* **2012,** *7* (3), 185-190.
53. Abbott, J.; Ye, T. Y.; Qin, L.; Jorgolli, M.; Gertner, R. S.; Ham, D.; Park, H., CMOS nanoelectrode array for all-electrical intracellular electrophysiological imaging. *Nature Nanotechnology* **2017,** *12* (5), 460-466.
54. Zhao, W.; Hanson, L.; Lou, H.-Y.; Akamatsu, M.; Chowdary, P. D.; Santoro, F.; Marks, J. R.; Grassart, A.; Drubin, D. G.; Cui, Y.; Cui, B., Nanoscale manipulation of

membrane curvature for probing endocytosis in live cells. *Nat Nanotechnol* **2017,** *12* (8), 750-756.
55. Caprettini, V.; Huang, J.-A.; Moia, F.; Jacassi, A.; Gonano, C. A.; Maccaferri, N.; Capozza, R.; Dipalo, M.; De Angelis, F., Enhanced Raman Investigation of Cell Membrane and Intracellular Compounds by 3D Plasmonic Nanoelectrode Arrays. *Advanced Science* **2018,** *5* (12), 1800560.
56. Huang, J.-A.; Caprettini, V.; Zhao, Y.; Melle, G.; Maccaferri, N.; Deleye, L.; Zambrana-Puyalto, X.; Ardini, M.; Tantussi, F.; Dipalo, M.; De Angelis, F., On-Demand Intracellular Delivery of Single Particles in Single Cells by 3D Hollow Nanoelectrodes. *Nano Letters* **2019,** *19* (2), 722-731.
57. Obien, M. E. J.; Deligkaris, K.; Bullmann, T.; Bakkum, D. J.; Frey, U., Revealing neuronal function through microelectrode array recordings. *Frontiers in Neuroscience* **2015,** *8*, 423.
58. Abbott, J.; Ye, T.; Krenek, K.; Gertner, R. S.; Ban, S.; Kim, Y.; Qin, L.; Wu, W.; Park, H.; Ham, D., A nanoelectrode array for obtaining intracellular recordings from thousands of connected neurons. *Nature Biomedical Engineering* **2020,** *4* (2), 232-241.
59. Spira, M. E.; Hai, A., Multi-electrode array technologies for neuroscience and cardiology. *Nat Nanotechnol* **2013,** *8* (2), 83-94.
60. Xie, C.; Liu, J.; Fu, T.-M.; Dai, X.; Zhou, W.; Lieber, C. M., Three-dimensional macroporous nanoelectronic networks as minimally invasive brain probes. *Nature Materials* **2015,** *14* (12), 1286-1292.
61. Dai, X.; Zhou, W.; Gao, T.; Liu, J.; Lieber, C. M., Three-dimensional mapping and regulation of action potential propagation in nanoelectronics-innervated tissues. *Nat Nanotechnol* **2016,** *11* (9), 776-782.
62. Hai, A.; Shappir, J.; Spira, M. E., In-cell recordings by extracellular microelectrodes. *Nat Methods* **2010,** *7* (3), 200-U50.
63. Hai, A., Ada Dormann, Joseph Shappir, Shlomo Yitzchaik, Carmen Bartic, Gustaaf Borghs, J. P. M. Langedijk, and Micha E. Spira., Spine-Shaped Gold Protrusions Improve the Adherence and Electrical Coupling of Neurons with the Surface of Micro-Electronic Devices. *Journal of The Royal Society Interface* **2009,** *6* (41), 1153–1165.
64. Langer, J.; Jimenez de Aberasturi, D.; Aizpurua, J.; Alvarez-Puebla, R. A.; Auguié, B.; Baumberg, J. J.; Bazan, G. C.; Bell, S. E. J.; Boisen, A.; Brolo, A. G.; Choo, J.; Cialla-May, D.; Deckert, V.; Fabris, L.; Faulds, K.; García de Abajo, F. J.; Goodacre, R.; Graham, D.; Haes, A. J.; Haynes, C. L.; Huck, C.; Itoh, T.; Käll, M.; Kneipp, J.; Kotov, N. A.; Kuang, H.; Le Ru, E. C.; Lee, H. K.; Li, J.-F.; Ling, X. Y.; Maier, S. A.; Mayerhöfer, T.; Moskovits, M.; Murakoshi, K.; Nam, J.-M.; Nie, S.; Ozaki, Y.; Pastoriza-Santos, I.; Perez-Juste, J.; Popp, J.; Pucci, A.; Reich, S.; Ren, B.; Schatz, G. C.; Shegai, T.; Schlücker, S.; Tay, L.-L.; Thomas, K. G.; Tian, Z.-Q.; Van Duyne, R. P.; Vo-Dinh, T.; Wang, Y.; Willets, K. A.; Xu, C.; Xu, H.; Xu, Y.; Yamamoto, Y. S.; Zhao, B.; Liz-Marzán, L. M., Present and Future of Surface-Enhanced Raman Scattering. *Acs Nano* **2020,** *14* (1), 28-117.
65. Ge, Q.; Li, Z.; Wang, Z.; Kowsari, K.; Zhang, W.; He, X.; Zhou, J.; Fang, N. X. J. I. J. o. E. M., Projection micro stereolithography based 3D printing and its applications. **2020,** *2* (2), 022004.
66. Harinarayana, V.; Shin, Y. C., Two-photon lithography for three-dimensional fabrication in micro/nanoscale regime: A comprehensive review. *Optics & Laser Technology* **2021,** *142*, 107180.

67. Lubin, S. M.; Zhou, W.; Hryn, A. J.; Huntington, M. D.; Odom, T. W., High-Rotational Symmetry Lattices Fabricated by Moire Nanolithography. *Nano Letters* **2012,** *12* (9), 4948-4952.
68. Zhou, W.; Gao, H. W.; Odom, T. W., Toward Broadband Plasmonics: Tuning Dispersion in Rhombic Plasmonic Crystals. *Acs Nano* **2010,** *4* (2), 1241-1247.
69. Zhang, S.; Zhang, Z.; Chen, S.; Zhu, R., Measurement of Electric Double Layer Capacitance Using Dielectrophoresis-Based Particle Manipulation. *Analytical Chemistry* **2021,** *93* (14), 5882-5889.
70. Joo, T. H.; Kim, M. S.; Kim, K., Surface-enhanced Raman scattering of benzenethiol in silver sol. *J. Raman Spectrosc.* **1987,** *18* (1), 57-60.
71. Inagaki, M.; Isogai, T.; Motobayashi, K.; Lin, K.-Q.; Ren, B.; Ikeda, K., Electronic and vibrational surface-enhanced Raman scattering: from atomically defined Au(111) and (100) to roughened Au. *Chemical Science* **2020,** *11* (36), 9807-9817.
72. Nam, W.; Zhao, Y.; Song, J.; Ali Safiabadi Tali, S.; Kang, S.; Zhu, W.; Lezec, H. J.; Agrawal, A.; Vikesland, P. J.; Zhou, W., Plasmonic Electronic Raman Scattering as Internal Standard for Spatial and Temporal Calibration in Quantitative Surface-Enhanced Raman Spectroscopy. *The Journal of Physical Chemistry Letters* **2020,** *11* (22), 9543-9551.
73. Madsen, S. J.; Esfandyarpour, M.; Brongersma, M. L.; Sinclair, R., Observing Plasmon Damping Due to Adhesion Layers in Gold Nanostructures Using Electron Energy Loss Spectroscopy. *ACS Photonics* **2017,** *4* (2), 268-274.
74. Rose, A.; Hoang, T. B.; McGuire, F.; Mock, J. J.; Ciracì, C.; Smith, D. R.; Mikkelsen, M. H., Control of Radiative Processes Using Tunable Plasmonic Nanopatch Antennas. *Nano Letters* **2014,** *14* (8), 4797-4802.
75. Mock, J. J.; Hill, R. T.; Degiron, A.; Zauscher, S.; Chilkoti, A.; Smith, D. R., Distance-Dependent Plasmon Resonant Coupling between a Gold Nanoparticle and Gold Film. *Nano Letters* **2008,** *8* (8), 2245-2252.
76. Huang, Y.; Ma, L.; Hou, M.; Li, J.; Xie, Z.; Zhang, Z., Hybridized plasmon modes and near-field enhancement of metallic nanoparticle-dimer on a mirror. *Scientific Reports* **2016,** *6* (1), 30011.
77. Chen, S.; Zhang, Y.; Shih, T.-M.; Yang, W.; Hu, S.; Hu, X.; Li, J.; Ren, B.; Mao, B.; Yang, Z.; Tian, Z., Plasmon-Induced Magnetic Resonance Enhanced Raman Spectroscopy. *Nano Letters* **2018,** *18* (4), 2209-2216.
78. Chance, R. R.; Prock, A.; Silbey, R., Frequency shifts of an electric-dipole transition near a partially reflecting surface. *Physical Review A* **1975,** *12* (4), 1448-1452.
79. Alù, A.; Engheta, N., Input Impedance, Nanocircuit Loading, and Radiation Tuning of Optical Nanoantennas. *Physical Review Letters* **2008,** *101* (4), 043901.
80. Gesteland, R. C.; Howland, B.; Lettvin, J. Y.; Pitts, W. H., Comments on Microelectrodes. *Proceedings of the IRE* **1959,** *47* (11), 1856-1862.
81. Prehn, R.; Abad, L.; Sánchez-Molas, D.; Duch, M.; Sabaté, N.; del Campo, F. J.; Muñoz, F. X.; Compton, R. G., Microfabrication and characterization of cylinder micropillar array electrodes. *Journal of Electroanalytical Chemistry* **2011,** *662* (2), 361-370.
82. Mei, B.-A.; Munteshari, O.; Lau, J.; Dunn, B.; Pilon, L., Physical Interpretations of Nyquist Plots for EDLC Electrodes and Devices. *The Journal of Physical Chemistry C* **2018,** *122* (1), 194-206.
83. Sánchez-Molas, D.; Esquivel, J. P.; Sabaté, N.; Muñoz, F. X.; del Campo, F. J., High Aspect-Ratio, Fully Conducting Gold Micropillar Array Electrodes: Silicon Micromachining and

Electrochemical Characterization. *The Journal of Physical Chemistry C* **2012,** *116* (35), 18831-18846.
84. Decker, D.; Hempelmann, R.; Natter, H.; Pirrung, M.; Rabe, H.; Schäfer, K. H.; Saumer, M., 3D Nanostructured Multielectrode Arrays: Fabrication, Electrochemical Characterization, and Evaluation of Cell–Electrode Adhesion. *Adv Mater Technol-Us* **2019,** *4* (2), 1800436.
85. Chen, C.; Ran, B.; Wang, Z.; Zhao, H.; Lan, M.; Chen, H.; Zhu, Y., Development of micropillar array electrodes for highly sensitive detection of biomarkers. *RSC Advances* **2020,** *10* (67), 41110-41119.
86. Kaniusas, E., *Biomedical Signals and Sensors III, Linking Electric Biosignals and Biomedical Sensors*. Springer Publishing: 2019.
87. Bredar, A. R. C.; Chown, A. L.; Burton, A. R.; Farnum, B. H., Electrochemical Impedance Spectroscopy of Metal Oxide Electrodes for Energy Applications. *ACS Applied Energy Materials* **2020,** *3* (1), 66-98.
88. Hezard, T.; Laffont, L.; Gros, P.; Behra, P.; Evrard, D., Hg(II) trace electrochemical detection on gold electrode: Evidence for chloride adsorption as the responsible for the broad baseline. *Journal of Electroanalytical Chemistry* **2013,** *697*, 28-31.
89. Wu, J., Understanding the Electric Double-Layer Structure, Capacitance, and Charging Dynamics. *Chemical Reviews* **2022,** *122* (12), 10821-10859.
90. Safiabadi Tali, S. A.; Song, J.; Nam, W.; Zhou, W., Two-Tier Nanolaminate Plasmonic Crystals for Broadband Multiresonant Light Concentration with Spatial Mode Overlap. *Advanced Optical Materials* **2021,** *9* (10), 2001908.
91. Johnson, P. B.; Christy, R. W., Optical Constants of the Noble Metals. *Physical Review B* **1972,** *6* (12), 4370-4379.

Chapter 4. Conclusions

This thesis elucidates the optical properties of fixed-size tapered-shape nanolaminate nanoantennas composed of vertically stacked MIM plasmonic building blocks. We revealed a tunable double-resonant optical responses achieved through out-of-plane engineering of metal-to-insulator thickness ratio via thin-film deposition. Numerical studies reveal the nature of two magnetoelectric modes resulting from hybridization of elementary modes in vertically stacked MIM building blocks, providing large resonant optical cross-sections, significant field enhancements, and broad spectral tunability in the visible-to-near-infrared regime. Such nanoantennas with compact footprint and high tunability are suitable for direct integration with other nanodevices, especially in nano-bio interfacing applications.

Following the study on the nanoantennas, we sought out to developed a procedure to pattern nanolaminate nanoantennas on micropillar electrode arrays, which enabled tunable hybrid optical-electrical functionality in a single device. We demonstrated how the optical and electrical functionality depends on structural geometry (controlled by micropillar diameter and PVD deposition thickness). Furthermore, experimental and calculated far-field optical spectra reveal multiple resonant plasmonic modes that can couple with the underlying conductive media of the electrodes, providing another mechanism by which to boost absorption cross section of optical nanoantennas. Near-field 2D maps show enhanced magnetic field intensities within dielectric nanocavities, that can be further exposed to the environment via dielectric wet chemical etching.

Electrochemical impedance spectroscopy and cyclic voltammetry provide insights into area-dependent microscopic electrochemical dynamics.